UNIVERSIDADE FEDERAL DE SANTA CATARINA
CENTRO TECNOLÓGICO
PROGRAMA DE PÓS-GRADUAÇÃO EM ENGENHARIA ELÉTRICA

Eduardo Pedó Gutkoski

Noise modeling in low-cost MEMs IMU sensors using experimental data

Florianópolis
2022

Eduardo Pedó Gutkoski

Noise modeling in low-cost MEMs IMU sensors using experimental data

Dissertation presented in partial fulfillment of the requirements for the degree of Master in Electrical Engineering.
Advisor: Prof. Anderson Wedderhoff Spengler, Dr.
Universidade Federal de Santa Catarina

Florianópolis
2022

Ficha de identificação da obra elaborada pelo autor,
através do Programa de Geração Automática da Biblioteca Universitária da UFSC.

Pedó Gutkoski, Eduardo
Noise modeling in low-cost MEMs IMU sensors using experimental data / Eduardo Pedó Gutkoski ; orientador, Anderson Wedderhoff Spengler, 2022.
70 p.

Dissertação (mestrado) - Universidade Federal de Santa Catarina, Centro Tecnológico, Programa de Pós-Graduação em Engenharia Elétrica, Florianópolis, 2022.

Inclui referências.

1. Engenharia Elétrica. 2. Unidades de medição inercial. 3. MEMS. 4. Ruído. I. Wedderhoff Spengler, Anderson. II. Universidade Federal de Santa Catarina. Programa de Pós Graduação em Engenharia Elétrica. III. Título.

Eduardo Pedó Gutkoski

Noise modeling in low-cost MEMs IMU sensors using experimental data

The present work at Master's level was evaluated and approved by an examining board composed of the following members:

Prof. Eduardo Augusto Bezerra, PhD.
Universidade Federal de Santa Catarina

Prof. Rodrigo Moreira Bacurau, Dr.
Universidade Estadual de Campinas

Prof. Flávio José de Oliveira Morais , Dr.
Universidade Estadual Paulista

We certify that this is the original and final version of the conclusion work that has been judged suitable for obtaining the title of Master in Electrical Engineering.

Documento assinado digitalmente
Telles Brunelli Lazzarin
Data: 21/06/2022 15:18:14-0300
CPF: 023.400.719-25
Verifique as assinaturas em https://v.ufsc.br

Prof. Telles Brunelli Lazzarin, Dr.
Graduate program coordinator

Documento assinado digitalmente
Anderson Wedderhoff Spengler
Data: 21/06/2022 15:09:24-0300
CPF: 052.275.659-02
Verifique as assinaturas em https://v.ufsc.br

Prof. Anderson Wedderhoff Spengler, Dr.
Universidade Federal de Santa Catarina
Advisor

Florianópolis, 24th march 2022.

To my family, especially my parents who give me support
for the fulfillment of my dreams.

ACKNOWLEDGEMENTS

First of all, I would like to thank my family, who with love and hard work have given me the necessary tools to achieve my goals, I will never be able to give you back this effort. Also, I want to thank my advisor, Prof. Anderson, for the possibility of working under his guidance, for the knowledge transmitted, and for the attention received during this work. Lastly, I am grateful to my colleagues Vitor Engers and Raphael Comesanha, for the support that was essential for this work.

This work was conducted during a scholarship supported by CNPq at the Federal University of Santa Catarina.

“Who is more humble? The scientist who looks at the universe with an open mind and accepts whatever the universe has to teach us, or somebody who says everything in this book must be considered the literal truth and never mind the fallibility of all the human beings involved?"
(Carl Sagan)

RESUMO

Os sistemas embarcados estão presentes em um grande número de veículos e dispositivos que realizam a navegação inercial. Os sensores embarcados atuais do tipo MEMS (sistemas microeletromecânicos) possuem grande acurácia em dados como posição, velocidade e atitude quando analisadas em um curto intervalo de tempo, porém, ao aumentar o intervalo, a confiabilidade dos dados integrados são degradadas rapidamente. Uma ferramenta importante para estimar a posição em um sistema de navegação é a modelagem dos componentes de ruído dos sensores nas unidades de medição inerciais (IMU). Essas unidades possuem diferentes classes de desempenho com elevado custo para um maior nível de acurácia, o que pode ser um problema para projetos com orçamento limitado, no entanto, uma solução é utilizar a redundância de sensores de baixo custo, de modo a se aproximar dos níveis de ruídos de sensores de classe maior. Neste trabalho foram avaliados os dados experimentais de giroscópios integrados em sensores IMU de baixo custo e os ruídos do sinal de saída, utilizando a variância de Allan para levantamento dos parâmetros. Como resultado, foi gerado um modelo genérico para simulação de giroscópios com a finalidade de possibilitar análises de combinações complexas de giroscópios em trabalhos futuros, observando se houve ganho de desempenho. Além disso, avaliou-se a combinação de giroscópios, utilizando a disposição mecânica para efetuar a compensação de deriva de *offset drift*, melhorando o desempenho do sistema.

Palavras-chave: Unidades de medição inercial. MEMS. Ruído.

RESUMO EXPANDIDO

Introdução

Através de acelerômetros e giroscópios é possível medir movimentos translacionais e rotacionais a partir de uma estrutura referenciada, o que é conhecido como navegação inercial. Atualmente inúmeros sistemas utilizam a detecção de movimento para atingir um alto nível de autonomia nos sistemas de navegação, por isso, os sensores de medição inercial podem ser encontrados em diversos contextos, desde equipamentos industriais a aparelhos eletrônicos pessoais, isso porque, o desenvolvimento tecnológico das últimas décadas transformou a indústria e possibilitou a utilização generalizada de sensores por inércia e com isso, a produção em massa a custos razoáveis. Para medir o movimento de um objeto é frequentemente utilizado uma unidade de medição inercial (IMU), com três giroscópios e três acelerômetros, pois um corpo rígido no espaço tridimensional tem seis graus de liberdade, três rotativos e três translacionais. Ainda que os avanços da tecnologia tenham melhorado significativamente a qualidade dos sensores inerciais, os sensores MEMS podem não satisfazer plenamente as necessidades de muitas aplicações que necessitam de um controle mais preciso, visto que estes sofrem com os efeitos da deriva dinâmica, não linearidades e instabilidade térmica nos sensores contemporâneos. Para mitigar estes efeitos de ruído dos sensores MEMS, uma solução é a utilização de matrizes IMU, nas quais as combinações redundantes de sensores podem resultar em medições mais assertivas.

Objetivos

O principal objetivo deste trabalho é realizar a coleta de dados experimentais de giroscópios em IMUs e emular o comportamento dos respectivos dados em um modelo matemático previamente desenvolvido e com isso validar a correlação entre os dados de saída do modelo e os dados experimentais. Os objetivos específicos contemplam a caracterização dos fatores de ruídos em IMUs de médio e baixo custo, a utilização do modelo para gerar dados simulados das IMUs caracterizadas, avaliação da similaridade entre os resultados de saída do modelo e os dados experimentais analisados, realização de combinações simples de IMUs com diferentes disposições mecânicas para avaliar se houve ganho de desempenho.

Metodologia

O conjunto material utilizado neste trabalho pode ser divido entre componentes de hardware e ‘software’. Foram utilizados três sensores IMU do tipo MEMS, sendo Murata SCC2130, Bosch BNO055 e Invensense MPU9250 e um microcontrolador Tiva-C TM4C123GXL, além de duas placas de circuito impresso desenvolvidas especialmente para este trabalho. Com relação ao ‘software’, o Code Composer Studio foi associado ao SDK da Tivaware para desenvolver o firmware. O processamento e visualização de dados foi feito através do Matlab, enquanto modelo foi gerado no Simulink e o LabView possibilitou a implementação do algoritmo de variação Allan. A aquisição dos dados de giroscópios de modo estacionário foi realizada via UART com o uso de um cabo USB. O firmware do microcontrolador foi implementado com uma leitura por temporização com interrupção para garantir a escolha da taxa de amostragem. Com relação ao modelo genérico de giroscópio, seu desenvolvimento se deu no âmbito do Laboratório de Integração de Software e Hardware (LISHA/UFSC - Campus Joinville) em outro contexto de pesquisa e implementado neste trabalho, o qual possibilitou a geração dos dados dos sensores. Por fim, estudou-se a variância de Allan de modo a extrair os parâmetros de ruídos de ARW (Angle Random Walk) e BI (Bias Instability) que eram

perninentes para o trabalho.

Resultados e discussão

A aquisição de dados dos sensores IMU gerou três conjuntos de dados nomeados Dataset 1, Dataset 2 e Dataset 3, em diferentes momentos da pesquisa. O Dataset 1 foi um teste estático com os sensores SCC2130/2230, BNO055 e MPU9250 utilizando a primeira versão da placa, a uma taxa de amostragem de 500 Hz em uma sala fechada em temperatura ambiente, por 5 horas. No Dataset 2 testaram-se os sensores BNO055 and SCC2130/2230 com a segunda versão da placa em uma câmara termal e temperatura constante de 26 graus Celcius por 12 horas. O Dataset 3 teve os mesmo parâmetros do Dataset 2, com excessão da temperatura, que variou durante o período de 12 horas. Com a coleta desses conjuntos de dados, analisaram-se os dados brutos de velocidade angular e temperatura. A partir dos dados de velocidade angular aplicou-se o algoritmo de variância de Allan para extrair os parâmetros de ruídos por meio da observação de gráfico em escala logarítmica. Com os parâmetros definidos, foi possível implementar o modelo para cada um dos sensores e avaliar se os parâmetros de ruídos dos dados simulados seguiam o mesmo comportamento dos dados experimentais. Além disso, foi feita uma combinação entre os sensores iguais utilizando diferentes disposições mecânicas, onde um permaceu sobre a placa e outro embaixo da mesma, de modo a avaliar uma redução nos coeficientes de ruídos e, consequentemente, aumento na desempenho do sensor. Por fim, após todos os testes e análise dos dados, comprovamos que o modelo reproduz o comportamento dos parâmetros de ruídos quando submetido a temperaturas constantes, o que não ficou evidenciado quando aplicado temperaturas variavéis, visto que o modelo desconsidera a deriva térmica. No que se refere à combinação de IMUs, obte-se um ganho de cerca de $1/\sqrt{2}$, o que reduziu significamente a deriva dinâmica e o ARW.

Palavras-chave: Unidades de medição inercial. MEMS. Ruído.

ABSTRACT

Embedded systems are present in a large number of vehicles and devices that perform inertial navigation. Current embedded MEMS (microelectromechanical systems) sensors have great accuracy in data such as position, velocity, and attitude when analyzed over a short time interval, but as the interval increases, the reliability of the integrated data is rapidly degraded. An important tool for position estimation in a navigation system is the modeling of sensor noise components in inertial measurement units (IMU). These units have different performance classes with high costs for a higher level of accuracy, which can be a problem for projects with a limited budget, however, one solution is to use redundancy of low-cost sensors to approach the noise levels of higher class sensors. In this work, experimental data from gyroscopes integrated into low-cost IMU sensors were evaluated for the output signal noises, using Allan's variance to survey the parameters. As a result, a generic model for gyroscopes simulation was generated to allow the analysis of complex combinations of gyroscopes in future works, observing if there was a performance gain. In addition, the combination of gyroscopes was evaluated, using the mechanical arrangement to perform the offset drift compensation, improving the system performance.

Keywords: Inertial Measurement Units. MEMS. Noise.

LIST OF FIGURES

Figure 1 – Simple accelerometer [5] 21
Figure 2 – Single mass gyroscope [12] 22
Figure 3 – Gyroscope performance grades [12] 23
Figure 4 – Part count reduction during the years [5] 24
Figure 5 – Coriolis effect on a single mass gyro [8]. 25
Figure 6 – Coriolis effect on turning fork configuration gyro [8]. 25
Figure 7 – $\sigma(\tau)$ plot for angle random walk [11] 30
Figure 8 – $\sigma(\tau)$ plot for Bias Instability [11] 31
Figure 9 – $\sigma(\tau)$ plot for rate random walk. [11] 31
Figure 10 – $\sigma(\tau)$ Plot for rate ramp [11] 32
Figure 11 – $\sigma(\tau)$ sample plot of Allan variance analysis [11] 33
Figure 12 – Estimated trajectories for 10 walks, showing the difference between taking single IMU measurements versus using an IMU array mean. [23] 35
Figure 13 – TivaC Launchpad [6] 38
Figure 14 – PCB Schematic first version 38
Figure 15 – PCB Schematic second version 39
Figure 16 – SCC2130 Block Diagram [3] 39
Figure 17 – BNO055 Architecture [13] 40
Figure 18 – MPU9250 Block Diagram [17] 40
Figure 19 – Hardware design diagram 41
Figure 20 – General firmware flowchart 42
Figure 21 – General software flow 42
Figure 22 – System showing the model for each IMU, with its respective axis [7] 43
Figure 23 – Implemented model in Simulink representing a single-axis gyroscope [7] 43
Figure 24 – Gyroscope model parameters [7] 44
Figure 25 – Allan variance plot showing the calculation of the parameters [25] . . 45
Figure 26 – Allan variance plot showing the calculation of the parameters [12] . . 45
Figure 27 – Thermal chamber 47
Figure 28 – MPU9250 3-axis gyroscope experiment data 47
Figure 29 – MPU9250 experiment temperature 48
Figure 30 – BNO055 3-axis gyroscope experiment data in time 48
Figure 31 – Temperature plots for BNO055 49
Figure 32 – SCC2130 X-axis gyroscope experiment data in time 49
Figure 33 – Temperature plots for SCC2130/2230 50
Figure 34 – Histogram showing the frequency that values appear on a 100 acquisition data for the sensors 50

Figure 35 – MPU9250 Gyro Allan variance result 51
Figure 36 – Dataset 2 BNO055 Gyro Allan variance result for all axis 53
Figure 37 – Dataset 3 BNO055 Gyro Allan variance result for all axis 54
Figure 38 – Dataset 1 SCC2230 gyroscope Allan variance result for Z-axis 56
Figure 39 – Dataset 2 SCC2130/2230 gyroscope Allan variance result for X/Z axis 57
Figure 40 – Dataset 3 SCC2130/2230 gyroscope Allan variance result 58
Figure 41 – Configuration blocks for the MPU9250 axis 59
Figure 42 – MPU9250 Gyro Allan variance result for the model, comparing with the real data results 59
Figure 43 – Comparison of AVAR from acquisition (all axis) and datasheet (x-axis) 60
Figure 44 – Configuration blocks for the BNO055 axis 60
Figure 45 – BNO055 gyroscope Allan variance result for the model, comparing with the real data results 61
Figure 46 – Comparison of AVAR from acquisition (all axis) and datasheet parameters 61
Figure 47 – Configuration blocks for the SCC2130 X-axis 62
Figure 48 – SCC2130 Gyroscope Allan variance result for the model, comparing with the real data results 62
Figure 49 – SCC2130 Gyroscope datasheet Allan variance [3] 63
Figure 50 – Comparison of AVAR from acquisition, simulation and datasheet . . . 63
Figure 51 – Illustration to represent the position of the sensors in relation to the board 64
Figure 52 – Dataset 2 BNO055 gyroscope for all axis Alan variance 64
Figure 53 – Dataset 1 2230 gyroscope Allan variance data combination 65

LIST OF TABLES

Table 3 – Performance Grades of Inertial Sensors [12] 23
Table 4 – Sensor data acquisition parameters 41
Table 5 – AVAR analysis parameter values for Figure 35 52
Table 6 – AVAR analysis parameter values for Figure 36 53
Table 7 – AVAR analysis parameters values for Figure 37 55
Table 8 – AVAR analysis parameters values for Figure 38 56
Table 9 – AVAR analysis parameters values for Figure 39 57
Table 10 – AVAR values for the SCC2130 datasheet 63
Table 11 – AVAR analysis parameters values for Figure 52 65
Table 12 – AVAR analysis parameters values for for Figure 53 66

LIST OF ABBREVIATIONS AND ACRONYMS

ADC	Analog-to-digital converter
ARW	Angle random walk
AVAR	Allan variance
BI	Bias instability
BW	Bandwidth
CAN	Controller area network
I2C	Inter-integrated circuit
IMU	Inercial measurement unit
MCM	Multi-chip Module
MEMS	Micro-electromechanical systems
ND	Noise density
PCB	Printed circuit board
PSD	Power spectral density
SPI	Serial peripheral interface
SR	Sample rate
SRAM	Static random-access memory
UART	Universal asynchronous receiver-transmitter

LIST OF SYMBOLS

g	Gravitational acceleration
F	Non-gravitational force
Ω	Angular movement
F_c	Coriolis effect force
σ	Standard deviation
$S_\theta(f)$	Angle PSD
$S_\Omega(f)$	Rate PSD
τ	Cluster time
$\sigma(\tau)$	Allan deviation

CONTENTS

1	**INTRODUCTION**	**18**
1.1	OBJECTIVE	18
1.1.1	**General Objectives**	**18**
1.1.2	**Specific Objectives**	**19**
1.2	STRUCTURE	19
2	**LITERATURE REVIEW**	**20**
2.1	INERTIAL NAVIGATION	20
2.1.1	**Inertial sensors**	**20**
2.1.2	**Grades of Inertial Sensors**	**22**
2.2	MICRO-ELECTROMECHANICAL SENSORS	23
2.2.1	**MEMS Gyroscopes**	**24**
2.2.2	**MEMS Gyroscope model**	**25**
2.3	INERTIAL SENSOR ERROR AND NOISE CHARACTERISTICS	26
2.3.1	**Noise Density**	**26**
2.3.2	**Bias**	**26**
2.3.2.1	Bias Instability	26
2.3.2.2	Bias Repeatability or turn-on bias stability	27
2.3.2.3	Temperature bias	27
2.3.3	**Angle random walk**	**27**
2.3.4	**Quantization noise**	**28**
2.3.5	**Rate random walk**	**28**
2.3.6	**Rate ramp**	**28**
2.4	ALLAN VARIANCE	29
2.4.1	**AVAR analysis of Angle random walk**	**30**
2.4.2	**AVAR analysis of Bias instability**	**30**
2.4.3	**AVAR analysis of Rate random walk**	**31**
2.4.4	**AVAR analysis of Rate ramp**	**31**
2.4.5	**Combined effects of noise processes**	**32**
2.4.6	**Estimation quality of Allan variance**	**33**
2.5	INERTIAL SENSORS ARRAYS	34
2.6	RELATED WORKS	35
3	**MATERIALS AND METHODS**	**37**
3.1	INTRODUCTION	37
3.2	HARDWARE COMPONENTS	37
3.2.1	**Microcontroller and PCB**	**37**
3.2.2	**SCC2130/2230**	**39**
3.2.3	**BNO055**	**40**

3.2.4 MPU9250 40
3.3 SENSOR DATA ACQUISITION 41
3.4 SOFTWARE COMPONENTS 41
3.4.1 Generic gyroscope model in Simulink 43
3.5 ALLAN VARIANCE METHODOLOGY TO EXTRACT THE NOISE TERMS 44
4 TEST AND RESULTS 46
4.1 INTRODUCTION 46
4.2 TEST ENVIRONMENT 46
4.3 DATA ACQUISITION RESULTS 47
4.3.1 MPU9250 47
4.3.2 BNO055 48
4.3.3 SCC2130/2230 49
4.3.3.1 Turn-on bias variation effect 50
4.4 AVAR IMPLEMENTATION 50
4.4.1 MPU9250 Allan Variance noise analysis 51
4.4.2 BNO055 Allan Variance analysis 52
4.4.3 SCC2130/2230 Allan variance analysis 55
4.5 MODEL RESULTS 58
4.5.1 MPU9250 59
4.5.2 BNO055 60
4.5.3 SCC2130/2230 61
4.6 IMU COMBINATION 63
4.6.1 BNO055 combination 64
4.6.2 SCC2230 combination 65
5 CONCLUSION 67
5.1 FUTURE WORKS 67
BIBLIOGRAPHY 68

1 INTRODUCTION

The subject of navigation has become an increasingly complex science whose relevance can be seen through the multiple possible ways to reach the desired destination. With accelerometers and gyroscopes to measure translational and rotational movements with a referenced frame comes what is known as inertial navigation. [5]

In this context, many systems require motion detection to attain a high level of autonomy in navigation systems. Inertial measurement sensors may be used in a wide range of applications, from industrial production equipment to personal electronic gadgets. The development of Micro-electromechanical systems (MEMS) technology in the recent decade has transformed the industry, allowing for widespread usage of inertial sensors [22], also, they can now be mass-produced in huge quantities and at reasonable costs [21].

Inertial sensors are mostly used to measure object motion. The motion of an item is frequently measured using a sensor known as an inertial measurement unit (IMU) with three gyroscopes and three accelerometers because a rigid body in three-dimensional space has six degrees of freedom, three rotating, and three translational [24]. Even though development has pushed the performance limits of inertial sensor technology, contemporary low-cost MEMS sensors cannot fully meet the needs of many applications that require more precise control. These applications suffer from the effects of bias instability, nonlinearities, and thermal instability in contemporary sensors.

To counter these noise effects from MEMS sensors, applications have been using IMU arrays, where redundant sensors combined can result in better measurements. Multi-sensor fusion has been a popular research area, with various researchers exploring it. Recent advances in electronics have made it possible to integrate numerous redundant sensors into a variety of existing systems for a range of applications [21]. As the amount of sensor data grows, a new field of research has emerged to address the issues of their integration and fusion [2].

1.1 OBJECTIVE

The sections below are described the general objective and the specific objectives.

1.1.1 General Objectives

The main objective of this work is to collect experimental data from IMU gyroscopes and emulate their behavior in an existing developed model to validate whether the model output correlates with the experimental data.

1.1.2 Specific Objectives

- Characterize the experimental noise factors in low and medium-cost commercial IMUs (units to tens of dollars).
- Use the mathematical models to generate simulated data of each characterized IMUs.
- Evaluate whether the models follow the results of the experiments.
- Perform simple assembly experiments to evaluate the simple combination of low-cost IMUs on overall performance.

1.2 STRUCTURE

Chapter 2 gives an overview of the use of inertial sensors in navigation, explaining their grades of performance and evolution. Also, it includes more in-depth topics about electronic gyroscopes, inertial sensor error, noise characteristics, and the combination of sensors to mitigate noise.

Chapter 3 covers the materials and methods used in the work, showing details about the electronic boards and the sensors, also covering the software part, explaining the tools, and exemplifying the firmware used through a diagram. Details about the gyroscope model are shown and finally, the method of extraction of the parameters for an Allan variance plot is described.

Chapter 4 describes the tests and results, showing the test environment, the acquisition of data, the implementation of the Allan variance method to extract the noise terms from the results. Also, it covers the model parameters to simulate the experimental values and finishes with a combination of data from sensors on different axis to show how it can reduce the noise parameters values. Finally, Chapter 5 presents the conclusions and suggestions for future work.

2 LITERATURE REVIEW

2.1 INERTIAL NAVIGATION

Inertial navigation systems (INS) are operated upon the laws of classical mechanics as formulated by Isaac Newton, telling us that the motion of a body will continue uniformly in a straight line unless disturbed by an external force acting on the body, generating a proportional acceleration of the body. This acceleration can be determined using a device known as an accelerometer. An INS usually contains three of these sensors, measuring the acceleration on three axes and the sensors are commonly mounted mutually perpendicular to each other.

To navigate with our inertial reference frame, it is necessary to keep track of which direction the accelerometers are pointing at that moment. For that purpose, gyroscopic sensors are used to determine the motion of the body concerning the inertial reference frame, thus discovering the orientation of the accelerometers at all times.

Therefore, inertial navigation is the process of determining the position of a vehicle using measurements from gyroscopes and accelerometers. By combining these pieces of information, it is possible to define the translational motion of the vehicle within the inertial reference frame and so calculate its position. Also, INS is self-contained in the vehicle, meaning they do rely upon the availability of accurate knowledge of the vehicle position at the start of navigation [5].

2.1.1 Inertial sensors

Relative to inertial sensors, the accelerometer is very utilized. It uses a small mass known as proof or seismic mass to measure the force acting upon it, it would be not practical to determine the acceleration of a vehicle by measuring the total force upon it. A simple accelerometer is shown in fig1, the proof mass is connected via a spring to the case. When the instrument's case is subjected to acceleration, the proof mass, which has its own inertia, tends to resist and, as a result, the mass is displaced with regard to the body.

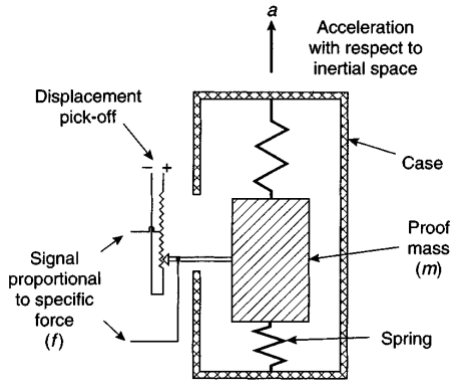

Figure 1 – Simple accelerometer [5]

It is important to notice that the accelerometer is insensitive to the gravitational acceleration (g), hence it provides an output proportional to the non-gravitational force per unit mass (F) to which the sensor is subjected along its axis. Taking an example of an accelerometer that is falling freely within the earth's gravitational field, the case and the proof mass will fall together, therefore the spring will not be extended. In this situation, the acceleration will be $a = g$ and the specific force is zero [5].

Another commonly used sensor is the magnetometer, responsible for measuring magnetic field intensity. It is an important sensor for components in aircraft and spacecraft, also it has been used widely in other sectors in the industry, biology, agriculture, etc. and nowadays almost no technology field is immune from magnetic measurements [15].

In the aeronautics field, magnetometers are used to measure geomagnetic field information of the position of the aircraft body, such as airplanes and satellites. Using a reference model for the earth's magnetic field and local magnetic field, it is possible to obtain the angle information of the body through an algorithm, therefore, the magnetometer is used in aircraft attitude and determination systems, especially in microsatellites, such as nanosatellites and picosatellites [31].

The geomagnetism can be applied in navigation for satellites in LEO (low-earth-orbit) with improvements for signal analysis, geomagnetic models, and processing technology [31]. The orbital elements can be acquired using a three-axis magnetometer to measure the three-dimensional component and the change rate of the geomagnetic field intensity vector, combining this with a Kalman filtering technology to calculate the estimated position and speed of the satellite afterward.

The sensor that will be the main focus in this work, the gyroscope is an inertial sensor that measures an object's angular rate with respect to an inertial reference frame, a simple model for the gyro is shown in Figure 2 [12]. It is used in applications to measure either the angle turned through by a vehicle or structure or its angular rate of turn in some defined axis. Some of the roles these sensors use include navigation, stabilization, flight path sensor, and autopilot feedback [5].

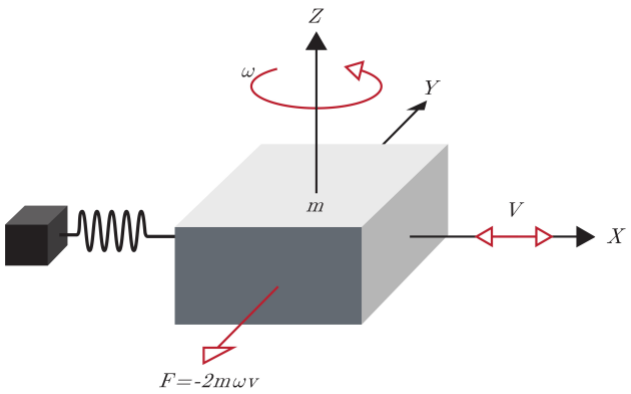

Figure 2 – Single mass gyroscope [12]

Many gyroscope sensors are strictly angular rate sensors and not gyroscopes, in the sense that they don't rely on the dynamical properties of rotating bodies. However, it has become accepted that all devices like such be referred to as a gyroscope since they all provide a measurement of body rotation [5].

2.1.2 Grades of Inertial Sensors

The inertial sensor market has an enormous range in terms of product price and performance. This variety can cause confusion for customers when determining the right component to select [12]. In general, inertial sensors can be grouped into one of the four performance categories [5]:

- Navigation Grade
- Tactical Grade
- Industrial Grade
- Automotive or Consumer Grade

For gyroscopes, there are many different types available, which range various levels of performance, including mechanical gyroscopes, ring laser gyroscopes (RLG), fiber-optic gyroscopes (FOGs), and quarts/MEMS gyroscopes as shown in Figure 3. In this work, MEMS gyroscopes will be utilized.

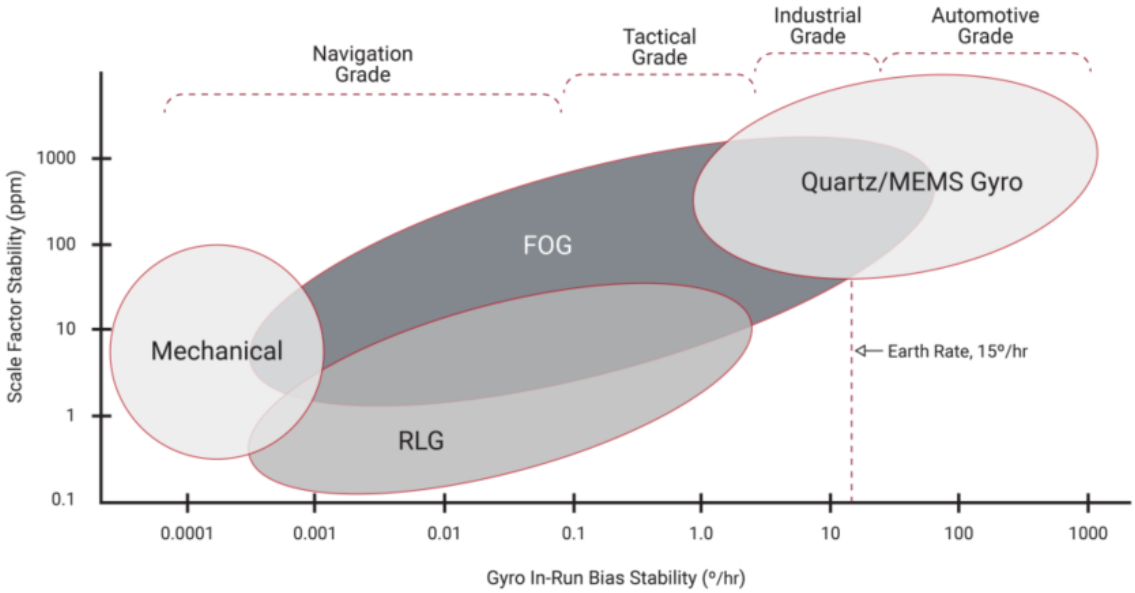

Figure 3 – Gyroscope performance grades [12]

These performance categories are based on the sensor's in-run bias stability, which is a key factor in determining inertial navigation performance. Many of the sensors in the Figure 3, with the exception of the mechanical gyroscope [5].

Grade	Cost	Gyro In-run Bias Stability	Application example
Consumer	10 $	-	Smartphones
Industrial	$100-$1000	10 deg/h	UAVs
Tactical	$5,000-$50,000	1 deg/h	Smart Munitions
Navigation	$100,000	0.1 deg/h	Military

Table 3 – Performance Grades of Inertial Sensors [12]

When deciding which grade of inertial sensor is suitable for a particular application, it's necessary to consider the level of accuracy required as well as the project's financial limits. As indicated in Table 3, the cost of inertial sensors rises as their performance grades improve. Consumer-grade inertial sensors are perfect for usage in smartphones and tablets because of their inexpensive cost. Navigation-grade inertial sensors, on the other hand, offer a far higher precision but a much higher cost, making them only practicable in the most mission-critical applications [12].

2.2 MICRO-ELECTROMECHANICAL SENSORS

The demand for low-cost sensors for new applications provided a major incentive for MEMS sensors. They are one of the most exciting developments in inertial sensors in the last 25 years [5]. The use of silicon as the base material in manufacturing overcomes many considered issues of conventional mechanical sensors, such as high count parts,

accurate testing and calibration, and assembly techniques, this is summarized in figure 4.

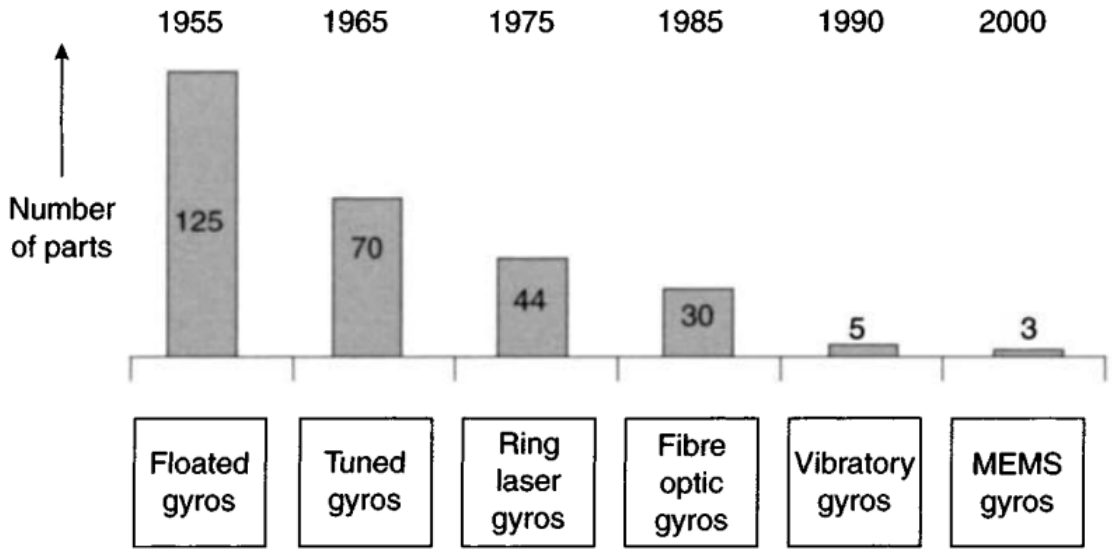

Figure 4 – Part count reduction during the years [5]

Due to the properties of silicon and the ease of developing high-fidelity components, these sensors evolved from a research device to a practical mass-volume sensor. However, when sensing devices shrink in size, new obstacles emerge for high-resolution and performance measurements, mostly due to sensitivity/scale-factor and noise increases; thermal sensitivity is also a concern [5].

2.2.1 MEMS Gyroscopes

MEMS gyroscopes are non-rotating devices that use the Coriolis acceleration effect on a vibrating proof mass to detect inertial angular rotation [5]. The Coriolis effect is shown in equation 1 and displayed in Figure 5, considering a mass moving in a direction with velocity v, when an angular movement (Ω) is applied, the mass m experiences a force in the direction of the yellow arrow as a result of the Coriolis effect (F_C). In MEMS gyroscope sensing, the resulting physical displacement is read using a capacitive interface. [26]

$$F_C = -2m(\omega_Z * v) \tag{1}$$

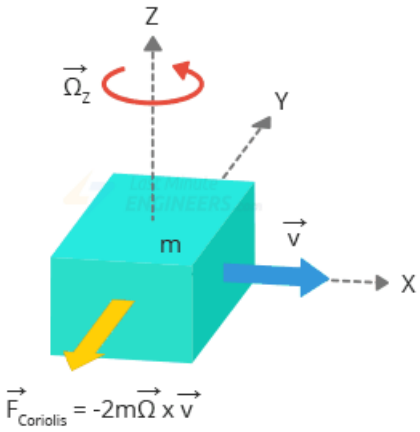

Figure 5 – Coriolis effect on a single mass gyro [8].

In a turning fork configuration (Figure 6), assume that two masses are kept in a continual oscillating motion so that they move in opposing directions at all times. When the angular rate is applied, the Coriolis force on each mass occurs in opposing directions, resulting in a change in capacitance between them, which is measured.

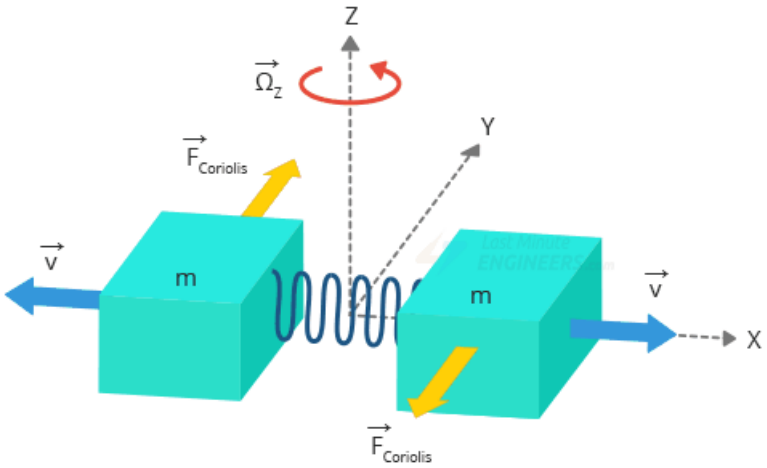

Figure 6 – Coriolis effect on turning fork configuration gyro [8].

The available MEMS gyros can be classified as follows: vibrating plates, vibrating beams, vibrating shells, and tuning fork [16]. The operating principle for all of them is the same. According to [21], MEMS-based gyroscopes dominate the 5 to 100 deg/h gyro market, and over the next decade will dominate the 100 to 0.1 deg/h range.

2.2.2 MEMS Gyroscope model

In order to create a realistic simulation of the sensor's behaviors, the parameters of the gyroscope shall be compared with a mathematical model [28]. The model includes

effects of dynamic bias, determined by the random walk effect. The angular velocity provided by the model is expressed by:

$$\omega_g = \omega + b_g + \beta_g + \eta_g, \tag{2}$$

in which ω is the real angular velocity, β_g and b_g are the gyroscope bias that can be separated in a fixed and time-varying bias, known as bias instability. Lastly, η_g is a zero-mean Gaussian white noise.

2.3 INERTIAL SENSOR ERROR AND NOISE CHARACTERISTICS

This section will go over the most prevalent inertial sensor errors and noises, as well as their influence on the output signal.The bias instability, angle random walk (gyroscope), quantization, rate angle walk, and rate ramp are the most frequent sources of error and noise.

2.3.1 Noise Density

Averaging a noisy signal and outputting it at a lower rate, known as downsampling, reduces the measured noise of sensor output. A single noise standard deviation is insufficient to properly characterize the inherent noisiness of a sensor, some datasheets will specify that standard deviation at a particular sample rate, however, the more common measure is noise density which provides the noise divided by the square root of the sampling rate [12]. The noise density of a gyroscope can be represented by ($°/s/\sqrt{Hz}$). By multiplying the Noise density (ND) by the square root of the Sample rate (SR) the standard deviation (σ) can be recovered ($\sigma = ND\sqrt{SR}$). Also, sometimes noise density is specified as power spectral density, which is the noise density squared, in gyroscope this yields the units of $(°/s)^2/\sqrt{Hz}$.

2.3.2 Bias

2.3.2.1 Bias Instability

Bias instability (BI) (also known as bias stability) is defined as how much deviation or drift the sensor has from its mean value of the output rate. This measurement tells how stable the bias of a sensor is over a certain period. Lower values are an advantage because it results in a sensor producing fewer deviations from the mean rate over time. This effect affects both gyros and accelerometers. The rate PSD associated with this noise is shown in equation 3, where B is the bias instability parameter and f_0

is the cutoff frequency.

$$S_{\Omega}(f) = \begin{cases} \frac{B^2}{2\pi}\frac{1}{f} & f <= f_0 \\ 0 & f > f_0 \end{cases} \tag{3}$$

2.3.2.2 Bias Repeatability or turn-on bias stability

When the sensor is started up, there is an initial bias present that can fluctuate in value from one turn-on to the next due to thermal, physical, mechanical, and electrical variations between measurements. Bias repeatability is the change in initial bias at constant conditions (eg. temperature) over the lifetime of the sensor, this change can't be calibrated during production, however, it can be estimated in an inertial navigation system after each startup. The turn-on bias stability is most relevant for unaided inertial navigation systems [12].

2.3.2.3 Temperature bias

When a sensor is used at a variety of temperatures, the bias may react differently to each of them. This is known as bias temperature sensitivity, and it can be calibrated after each of these biases has been measured throughout a temperature range. This bias, however, can only be measured within the bounds of bias instability [12].

2.3.3 Angle random walk

Angle random walk (ARW) is a noise specification with $degree/\sqrt{h}$ as units, that is directly applicable to the computation of angles. The ARW estimates the bias average deviation that will affect the integrated signal, which is mostly linked to the noise width. The samples obtained are disturbed by white noise as a consequence.

The associated rate noise Power spectral density (PSD) is associated by equation 4 where N is the angle random walk parameter expressed in $°/h/\sqrt{Hz}$, defining the output noise as a function of the sensor bandwidth.

$$S_{\omega}(f) = N^2. \tag{4}$$

Manufacturers usually specify noise specifications in various ways, in the form of ARW, PSD, or FFT noise density and with σ variations in the sensor output. Estimating the ARW with these parameters is described in the IEEE 952-1997 C.1.1 (equation 5, 6 and 7). In ARW:

$$N(°/\sqrt{h}) = \frac{1}{60}\sqrt{PSD[(°/h)]^2/Hz} \tag{5}$$

$$N(°/\sqrt{h}) = \frac{1}{60}FFT(°/h/\sqrt{Hz}) \tag{6}$$

$$N(°/\sqrt{h}) = \frac{1}{60}\sigma(°/h)\frac{1}{\sqrt{BW}(Hz)}, \tag{7}$$

where σ is the standard deviation of the signal in $°/h$, Bandwidth (BW) is the effective bandwidth of the sensor in Hz and FFT is the noise density in $°/h/\sqrt{Hz}$.

2.3.4 Quantization noise

Quantization noise is introduced into an analog signal that results from encoding it in digital form, it is caused by the small differences between the amplitudes of the points being sampled and the digital resolution of the analog to digital converter [9]. The angle PSD ($S_\theta(f)$) is given as (IEEE 952-1997) is

$$S_\theta(f) = \begin{cases} \tau_0 Q^2\{\frac{sin^2(\pi f\tau_0)}{(\pi f\tau_0)^2}\} \\ \approx \tau_0 Q^2 \qquad\qquad f < \frac{1}{2\tau_0}, \end{cases} \tag{8}$$

where Q is the quantization noise parameter and τ is the sample interval. Theoretically, the limit for Q is $S/\sqrt{12}$, where S is the gyro scaling factor for tests with uniform and fixed sample times [18]. The rate PSD $S_\Omega(f)$ is related to the angle PSD through the equation:

$$S_\Omega(2\pi f) = (2\pi f)^2 S_\theta(2\pi f), \tag{9}$$

Therefore,

$$S_\Omega(f) = \begin{cases} \frac{4Q^2}{\tau_0}\sin^2\pi f\tau_0 \\ \approx (2\pi f)^2\tau_0 Q^2 \quad f < \frac{1}{2\tau_0}. \end{cases} \tag{10}$$

2.3.5 Rate random walk

Rate random walk is a random process of uncertain origin, possibly a limiting case of an exponentially correlated noise with a very long correlation time [11]. The rate PSD associated with this noise is

$$S_\Omega(f) = (\frac{K}{2\pi})^2\frac{1}{f^2}, \tag{11}$$

where K is the rate random walk parameter.

2.3.6 Rate ramp

Using long time intervals the acquired data can indicate a change very slow monotonic intensity of the gyro source that persists over a long period of time. Also,

it could be due to a very small acceleration of the platform in the same direction and persisting for a long period of time [11]. It appears as an input to the gyro given:

$$\Omega = Rt, \tag{12}$$

where R is the ramp parameter.

The PSD associated with this noise is:

$$S_\Omega(f) = \frac{R^2}{(2\pi f)^3}. \tag{13}$$

2.4 ALLAN VARIANCE

Allan variance, also known as two-sample variance, is a technique developed by David W. Allan in 1966 to address the problem of crystal oscillators and atomic clocks not having a phase noise consisting of only white noise, but white frequency noise and flicker noise as well. These new noise forms became a challenge for the statistical tools at the time. A side consequence of having these types of noises was that the measurement methods did not agree with each other, so the key aspect of repeatability of measurements could not be achieved [1].

The two-sample variance provided a mean to separate many noise forms for time-series or frequency measurements between oscillators but did not completely allow all types of noises to be distinguished. In 1988, IEEE identified the two-sample variance as the preferred measure [10]. With the possibility of analyzing the noises separately, the technique was utilized in a lot of sample systems, as an example, the IEEE patterns for laser gyrometers indicate that Allan variance can be utilized as a unique method for data analysis or as a complement for other techniques in frequency analysis [10]. In this pattern, there is five types of noises analyzed by the technique: quantization noise, angle random walk, bias instability, and rate ramp.

For exemplification, considering N samples of gyro data with a sample rate of τ_0. Forming data clusters of lengths τ_0, $2\tau_0$, ..., $k\tau_0$ ($k < N/2$) and obtaining averages of the sum of data points contained in each cluster over the length of that cluster. The Allan variance is defined as a function of cluster time (τ).

$$\sigma(t) = \int^t \Omega(t')dt', \tag{14}$$

$$\Omega_k(\tau) = \frac{\theta_{k+m} - \theta_k}{\tau}, \tag{15}$$

where

$$\tau = m\tau_0.$$

The Allan variance is defined in equation 16. Note that $\langle\ \rangle$ is an ensemble average.

$$\sigma^2(\tau) = \frac{1}{2}\langle(\Omega_{k+m} - \Omega_k)^2\rangle. \tag{16}$$

The Allan variance is estimated as follows:

$$\sigma^2(\tau) = \frac{1}{2\tau^2(N-2m)} \sum_{k=1}^{N-2m} (\theta_{k+2m} - 2\theta_{k+m} + \theta_k)^2. \tag{17}$$

The relation between Allan variance and the two-sided PSD is shown in equation 18. This equation is key to calculate Allan variance from rate noise PSD [10].

$$\sigma^2(\tau) = 4\int_0^\infty S_\omega(f)\frac{sin^4(\pi f\tau}{(\pi f\tau)^2}df \tag{18}$$

2.4.1 AVAR analysis of Angle random walk

Using equations 18 and 4applying integration, yields equation 19. In figure 7 equation 19 indicates that a log plot of $\sigma(\tau)$ versus τ indicates a slope of -1/2 [11].

$$\sigma^2(\tau) = \frac{N^2}{\tau} \tag{19}$$

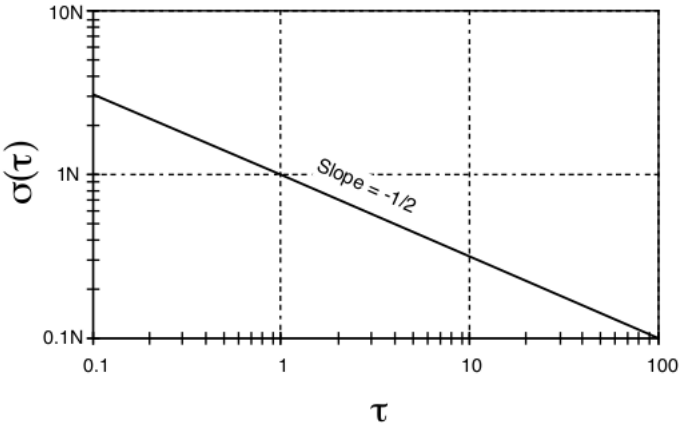

Figure 7 – $\sigma(\tau)$ plot for angle random walk [11]

2.4.2 AVAR analysis of Bias instability

The relation of bias instability in time is shown in 20, where $x = \pi f_0 \tau$ and C_i is the cosine-integral function. Figure 8 shows the log-log plot for this equation, the flat region of the plot can be examined to estimate the limit of the bias instability as well as the cutoff frequency of the underlying flicker noise [11].

$$\sigma^2(\tau) = \frac{2B^2}{\pi}[\ln(2) - \frac{\sin^3(x)}{2x^2}(\sin(x) + 4x\cos(x)) + C_i(2x) - C_i(4x)] \tag{20}$$

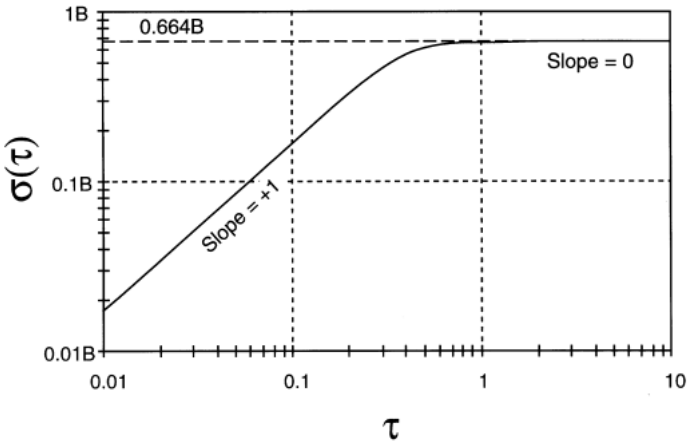

Figure 8 – $\sigma(\tau)$ plot for Bias Instability [11]

2.4.3 AVAR analysis of Rate random walk

Rate random walk is a process of uncertain origin, a limiting case of an exponentially correlated noise with a very long correlation time [11]. K is the rate random walk parameter, equation 21 shows the PSD associated with this noise.

$$S_{\Omega}(f) = (\frac{K}{2\pi})^2 \frac{1}{f^2} \tag{21}$$

Equation 22 shows the relation of K in time, also the K parameter can be obtained graphically (figure 9 by extrapolating the +1/2 slope curve and the curve value extrapolated to $\tau = 3$ hours will be the value of the magnitude (K).

$$\sigma^2(\tau) = \frac{K^2 \tau}{3} \tag{22}$$

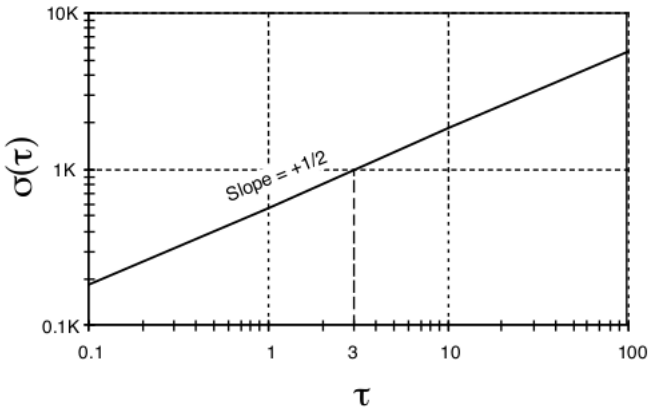

Figure 9 – $\sigma(\tau)$ plot for rate random walk. [11]

2.4.4 AVAR analysis of Rate ramp

This change will appear as an error in calculating Allan's Variance, and it is associated with the region where the slope will be +1, as shown in figure 10 [11].

R will be the rate ramp parameter and can be obtained by extending the curve of the region with +1 slope for the instant $\tau = \sqrt{2}$ hours and utilizing the value of $\theta(\tau)$ to express R, their relation is shown in equation 23. The PSD rate for rate ramp is shown in equation 24.

$$\sigma^2(\tau) = \frac{R^2\tau^2}{2} \tag{23}$$

$$S_\Omega(f) = \frac{R^2}{(2\pi f)^3} \tag{24}$$

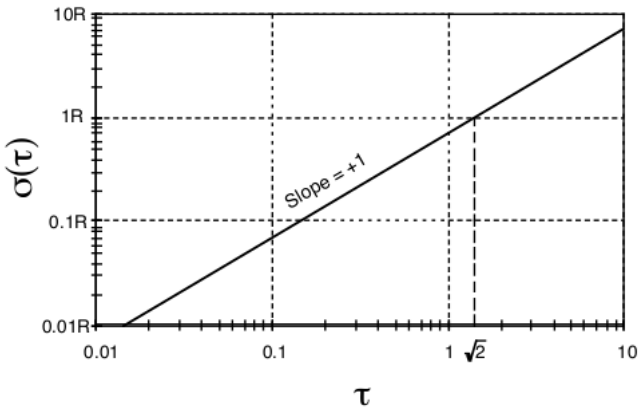

Figure 10 – $\sigma(\tau)$ Plot for rate ramp [11]

2.4.5 Combined effects of noise processes

A typical Allan variance plot looks like Figure 11. Experience shows that in most cases, different noise items appear in different regions of τ, allowing the identification of various random processes that exist in the data. It is assumed that the random processes existing in data are independent, as shown in equation 25 [11]. Figure 11 illustrates the noise parameters.

$$\sigma^2_{total}(\tau) = \sigma^2_{ARW}(\tau) + \sigma^2_{quant}(\tau) + \sigma^2_{BiasInst}(\tau) + \ldots \tag{25}$$

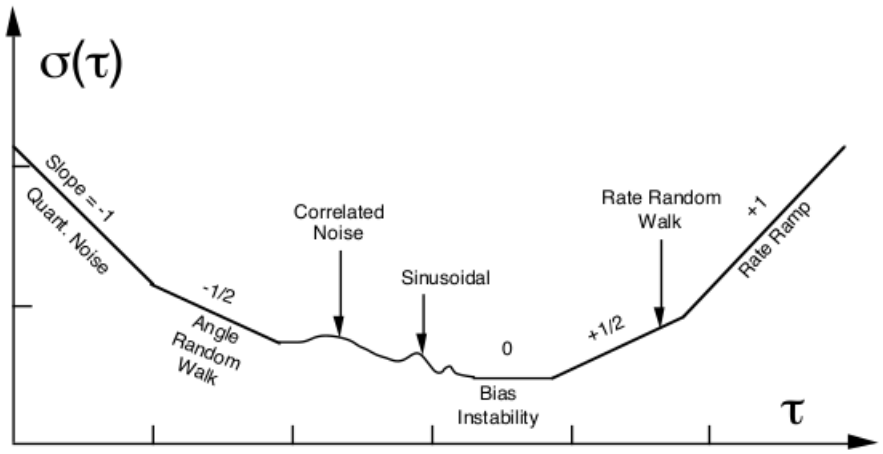

Figure 11 – $\sigma(\tau)$ sample plot of Allan variance analysis [11]

With real data, there are many subtle transitions between the various Allan standard deviation slopes. Because of the uncertainty of the measured Allan variance, some noise or hash in the plot curve is present [10].

2.4.6 Estimation quality of Allan variance

The Allan variance is estimated in practice using a finite number of independent clusters that can be constructed from any length of data. The total number of clusters of a particular length that can be produced is used to determine the Allan variance of any noise factor. As the number of independent clusters grows, so does the confidence in the estimation.

The parameter δ_{AV} is defined as the percentage inaccuracy in predicting the cluster's Allan standard deviation due to the finite number of clusters, gives [11]

$$\delta_{AV} = \frac{\sigma(T,M) - \sigma(T)}{\sigma(T)}, \tag{26}$$

where $\sigma(T,M)$ denotes the estimate of the Allan standard deviation obtained from M independent clusters, $\sigma(T,M)$ approaches its theoretical value, $\sigma(T)$, in the limit of M approaching infinity. In [20] ,the author presents a straightforward calculation that shows the percent error is equal to

$$\sigma(\delta_{AV}) = \frac{1}{\sqrt{2 * (\frac{N}{n} - 1)}}, \tag{27}$$

where N is the total number of data points in the entire data set, and n is the number of data points contained in the cluster.

Equation 27 demonstrates that when the number of independent clusters in these regions is large, the estimation of errors in the short T region is small. For example, if there are 100,000 data points and 10,000 cluster sizes are used, the percentage error

is expected to be around 23.5%. However, if 1000 data points are used with a cluster size of 10, the percentage of error is approximately 7.1%.

2.5 INERTIAL SENSORS ARRAYS

An inertial sensor array is a concept of combining redundant accelerometer and gyroscope sensing elements [19]. These arrays are utilized to bring increased qualities and capabilities that a non-redundant sensor assembly cannot provide. Using these arrays of Inercial measurement unit (IMU) allows for greater precision, realism, and uncertainty estimation.

The main objectives for IMU arrays research are measurement fusion, dealing with how to process and combine inertial measurements to attain estimates of angular velocity and specific forces or to attain higher-level information such as attitude and position. Calibration and error analysis deal with how to model, estimate and compensate for array imperfections, how errors affect the system, and lastly, sensor constellation geometry and the number of sensors to be used [19].

The work of Timothy Crain et al.[4], utilizes a larger number of IMUs with less accuracy to provide more robust measurements to compensate for the inherent error in each sensor, this concept is called the multi-sensor/single-functional(MSSF) paradigm. The swarm sensing is used to answer the question of whether a larger number of low-cost IMUs together can be equivalent to a single navigation grade IMU.

The authors found that matching or improving the measurements in a static comparison for navigation grade IMU with a pool of N sensors for acceleration measurement is not practicable. However, with a slight increase in mass, angular rate measurement from a MEMS-based swarm system is competitive with classic navigation grade IMU systems in terms of power [4].

In a navigation application for a GPS-denied environment, M. Tanenhaus et al. [27] utilize an array of MEMS inertial sensors to improve long-term accuracy. Their solution is integrated into a 100-sensor assembly with a dual-processor that can handle the sensors simultaneously at high sample rates. The basic foundation for achieving precision by using an array of sensors, according to the author, is to combine them in complementary pairs to reduce noise and drift. The approach is then extended to numerous layers of sensors to create a weighted combination of paired subarrays that is optimal. Moving from a single gyro to an array of eight lowered the ARW and Bias instability parameters values, according to the author. On a root-Allan variance plot, the improvement is visible.

In the article of Isaac Skog et al. [23], a navigation example of utilization of IMU arrays is introduced. The idea is to utilize multiple low-cost IMUs to track pedestrians in indoor environments where GPS and cellular or Wifi-based localization have insufficient accuracy and robustness because of the radio technology.

Their hardware consisted of an IMU-array platform that contained eighteen MPU9150, nine on the top side of the PCB and nine on the bottom side. The experiment results are shown in Fig. 12, which was obtained with an agent equipped with the IMU array in the sole of his shoes in ten 200m walks. Notice the discrepancy between single IMU measurements versus the mean of an IMU array [23].

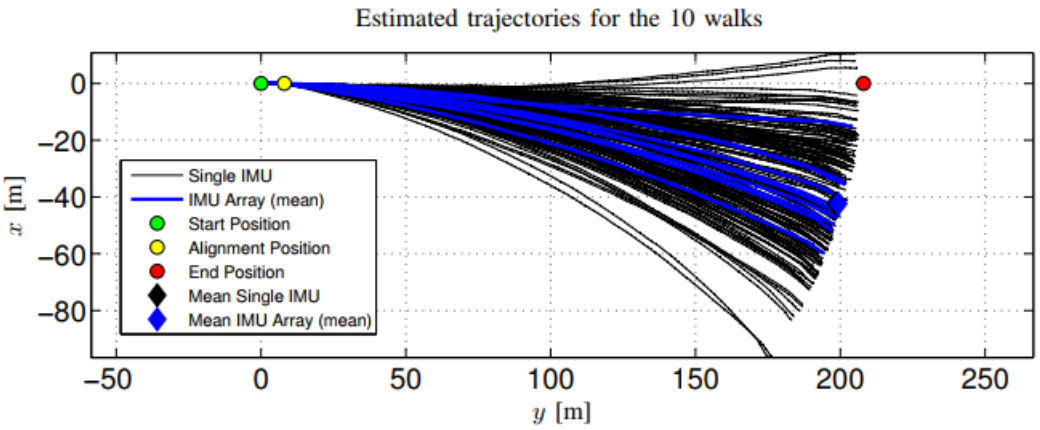

Figure 12 – Estimated trajectories for 10 walks, showing the difference between taking single IMU measurements versus using an IMU array mean. [23]

2.6 RELATED WORKS

This section presents the related work in the context of gyroscope models. In addition, there is a discussion around the gyroscope model used for each work.

In Carrara et. al [28], the authors describe the development of a model to characterize a gyroscope MPU3300 and a magnetometer HMC5843 that integrates a computer board of a nanosatellite and are employed in the Attitude Determination and Control Subsystem (ADCS). Three static tests with different configurations and one in a controlled rotation table were made to collect gyroscope and magnetometer data and characterize the noise parameters using Allan Variance. Their gyroscope the model included the effect of a dynamic bias, governed by a random walk effect, where the simulated angular velocity is the sum of a real angular velocity, a zero mean Gaussian white noise and a fixed and a time varying bias. After defining the model, the authors extracted the noise parameters from the tests to validate the model implementation with real values. They concluded that the gyroscope model showed a good agreement with the experimental values, except for the time constant on the x axis. Also, the model does not fully fit the measurements, which indicates the presence of a more complex noise pattern. For that reason, the gyroscope's behavior should be expected to be better than shown in the model.

In Xue et. al [30], the authors worked on the modeling of stochastic error for MEMS gyroscopes, usually, measurement errors contain both deterministic and stochastic errors, however, they only considered the latter. Their error model is similar to the

previous article, where the simulated angular rate is equal to a sum of the real input angular rate, a bias drift driven by noise of RRW (Rate Random Walk) and ARW (Angle Random Walk) white noise. To identify and quantify the stochastic noise of a MEMS gyroscope, the Allan variance method was employed. In addition, to reduce noise and bias drift, the authors designed an optimal Kalman filter by a steady-state filter gain obtained from the analysis of KF observability, the true angular rate signal was modeled to obtain an optimal estimate and make a self-compensation, whether in static or dynamic conditions. For the experiment, a low-performance and low-cost MEMS gyroscope ADXRS300 was utilized. Their filter approach reduced the ARW from $4.87°/\sqrt{h}$ to $0.4°/\sqrt{h}$ and Bias instability from $44.41°/h$ to $4.13°/h$ in one experiment, demonstrating that this approach can effectively reduce the measurement noise and accurately reflect the dynamic characteristic of the input signal.

In Lam et. al. [14], a unit scaling-based approach to model gyroscope random noise sources is presented. Also, the design and development of a ground-based software tool to extract the noise source values. The solution is implemented using Matlab/Simulink using the Power Spectral Density (PSD) and Allan Variance techniques, and its performance is validated using high fidelity data from experiments. The tools developed in the article were used to characterize on-orbit gyro noise performance for a star tracker/gyro-based attitude determination system. The employed model is the sum of a true rate, a gyro drift rate bias driven by the RRW process, and a white noise corrupting the gyro rate measurement. This model is employed for normal operations, for a mission that requires high rate or large angle slew operations, a higher fidelity model was proposed where were added the gyro scale factor and misalignment errors. The performance results indicate a direction in accurately estimating the values of gyro random noise sources, the success of the technique can be applied to enhance performance on the on-board satellite attitude determination system by updating the noise parameters into the on-board filter process noise matrix.

Concerning the related works presented above, the approach used in this work to characterize gyroscope noise sources follows the current literature and proposed solutions in general lines, especially the choice of Allan variance methodology and the method of data acquisition. Otherwise, we observed some differences between equation variables as the addition of the gyro scale factor, Rate Random Walk, and misalignment errors, for example.

3 MATERIALS AND METHODS

3.1 INTRODUCTION

The development of the work was done using three laboratories:

- Space Technology Research Laboratory - SpaceLab (UFSC Florianopolis), that has infrastructure for electronic projects with its focus on space applications, competitions, events, and academic research.
- Software/Hardware Integration Laboratory - LISHA (UFSC Joinville) is a laboratory that researches the frontier of hardware and software, dedicated to research in network and computer architecture, operating system, and embedded system applications.
- Instrumentation and Sensor Laboratory - LIS (UNICAMP), has infrastructure for electronic projects with a focus on sensors and instrumentation.

In this work, we tested three models of MEMS inertial sensors. All of them are digital sensors, i.e. sensors with analog-to-digital converters (ADCs) built into the sensor chip. They are Murata SCC2130, Bosch BNO055 and Invensense MPU9250 [3][13][17]. The IMUs were selected according to the models available at the Software and Hardware Integration Laboratory (LISHA) of the UFSC Joinville campus.

The sensors communicate either with serial peripheral interface (SPI) protocol or with inter-integrated-circuit (I2C) protocol, both allowing a large number of devices to communicate with a master device.

3.2 HARDWARE COMPONENTS

3.2.1 Microcontroller and PCB

The microcontroller used is the Tiva-C Launchpad TM4C123GXL (Figure 13), which is a low-cost evaluation platform that features an Arm Cortex-M4F CPU, 256kB of flash, and 32kb of Static random-access memory (SRAM), the kit also provides a USB 2.0 interface and two 12-bit ADC modules. The launchpad includes common serial communication protocols such as Universal asynchronous receiver-transmitter (UART), Serial peripheral interface (SPI), Inter-integrated circuit (I2C) and Controller area network (CAN) [6].

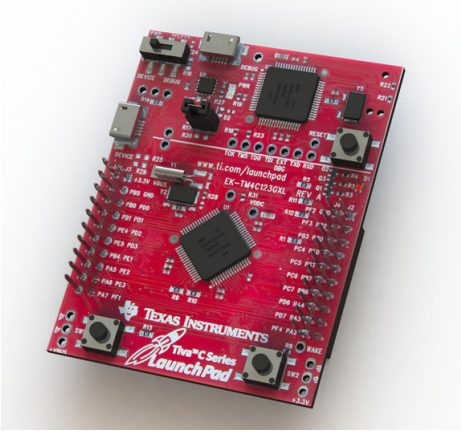

Figure 13 – TivaC Launchpad [6]

Throughout the work, two circuit boards were made, the first version contained 2 SCC2130, 2 BNO055, and 4 MPU9250, the schematic is shown in Figure 14. The second version, shown in Figure 14, has 6 SCC2130 and 4 BNO055. Both boards were designed in a way that there are half of the sensors on the upside of the board and half of the sensors on the bottom side. For context, we wanted to focus on two sensors that we had more success with tests, and to add more quantity of them to analyze their combination of data, therefore we developed a second board.

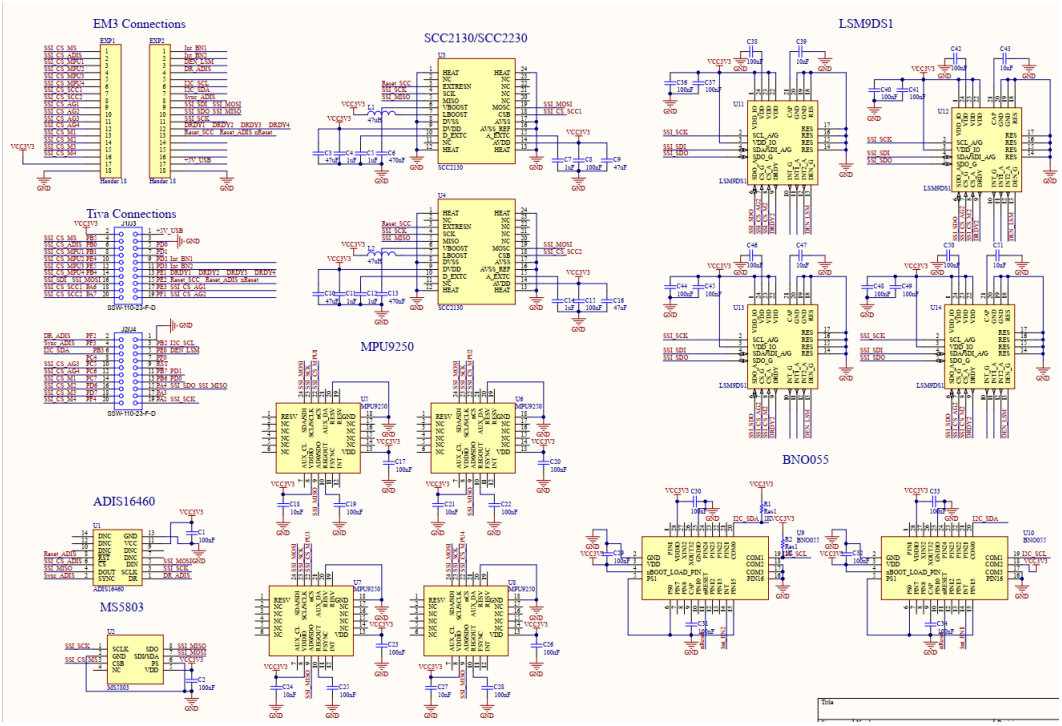

Figure 14 – PCB Schematic first version

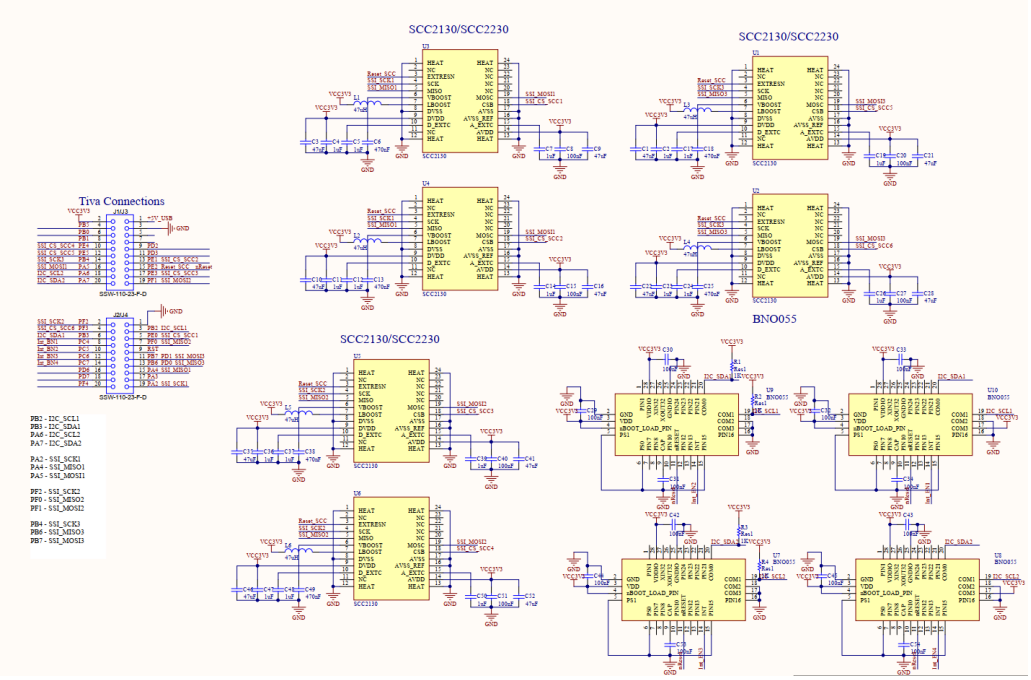

Figure 15 – PCB Schematic second version

3.2.2 SCC2130/2230

The SCC2130/SCC2230 (Figure 16) is a combined angular rate and accelerometer sensor manufactured by Murata. It consists of X-axis angular rate sensor and three-axis accelerometer sensor based on capacitive 3D-MEMS technology. The signal processing is done by an ASIC that provides angular rate and acceleration output via SPI digital interface. The gyro-in-run bias is 0.05, according to the datasheet [3].

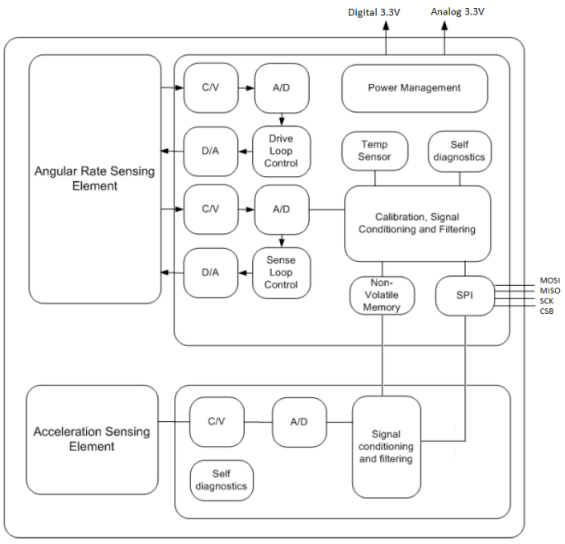

Figure 16 – SCC2130 Block Diagram [3]

3.2.3 BNO055

The BNO055 is a system in package (SiP) sensor that integrates a three-axis accelerometer, a triaxial gyroscope, a triaxial geomagnetic sensor, and a 32-bit microcontroller to do the signal processing and send the output data. It supports both SPI and I2C digital interfaces [13].

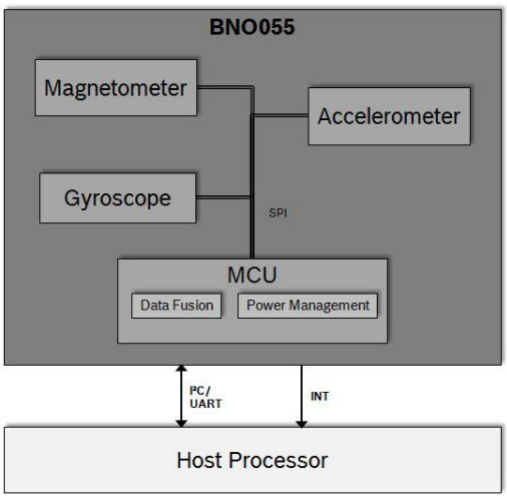

Figure 17 – BNO055 Architecture [13]

3.2.4 MPU9250

The MPU-9250 is an Multi-chip Module (MCM) sensor from InvenSense that consists of a triaxial gyroscope, a triaxial accelerometer, and a triaxial magnetometer, and a digital motion processor, with 16-bit Analog-to-digital converter (ADC) and signal conditioning. It supports I2C at 400kHz or SPI at 1 Mhz digital interface [17].

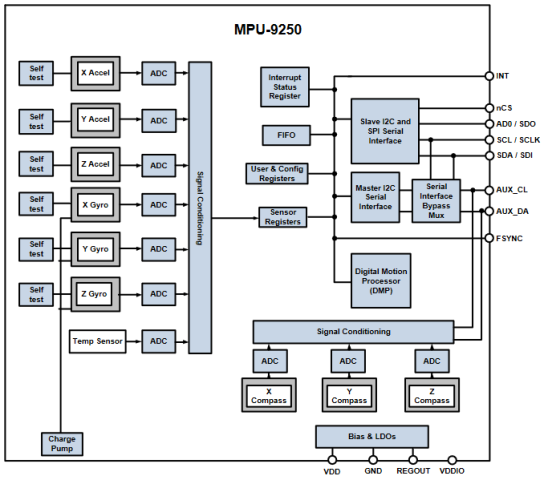

Figure 18 – MPU9250 Block Diagram [17]

3.3 SENSOR DATA ACQUISITION

The data acquisition was carried out in three datasets, called in this work Dataset 1, Dataset 2, and Dataset 3 according to table 4. The stationary acquisitions were done in a steady place via UART protocol with a USB cable. To further exemplify the hardware proposal, Figure 19 shows a diagram to demonstrate the protocols used for communicating the micro-controller with the sensors and the computer.

Sensor	Sample Rate (Hz)	Comm. Protocol	Dataset
SCC 2130/2230	500 and 50	SPI	1-2-3
BNO055	50	I2C	2-3
MPU 9250	500	SPI	1

Table 4 – Sensor data acquisition parameters

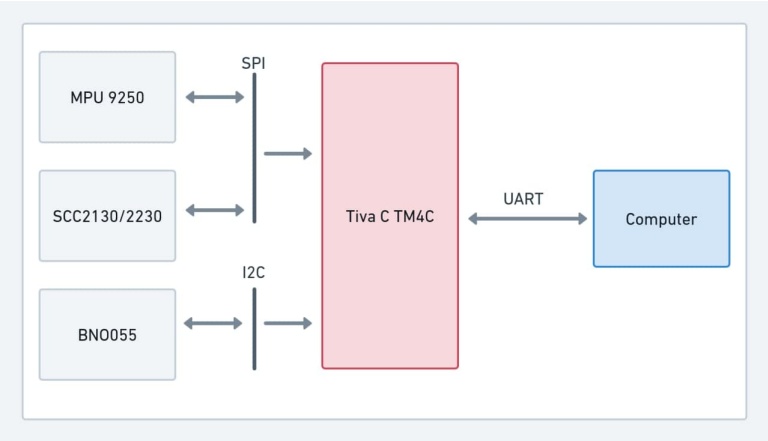

Figure 19 – Hardware design diagram

3.4 SOFTWARE COMPONENTS

The firmware was written in C using Code Composer Studio editor with the TivaWare development kit SDK. A general block diagram for the firmware is shown in Figure 20, this flowchart is similar to all sensors, only differing in the communication protocol for acquisition. The firmware initially configures the sensor programmable registers, such as the addition of digital filters to the output, also a check-up is done to guarantee that the sensor is working properly by reading certain registers. After this initialization, the timer interrupt routine is started, in this routine, the timer is adjusted to the desired sample time and the sensor data is read. If there is no error in the reading, the sensor data is transferred via UART through the USB cable.

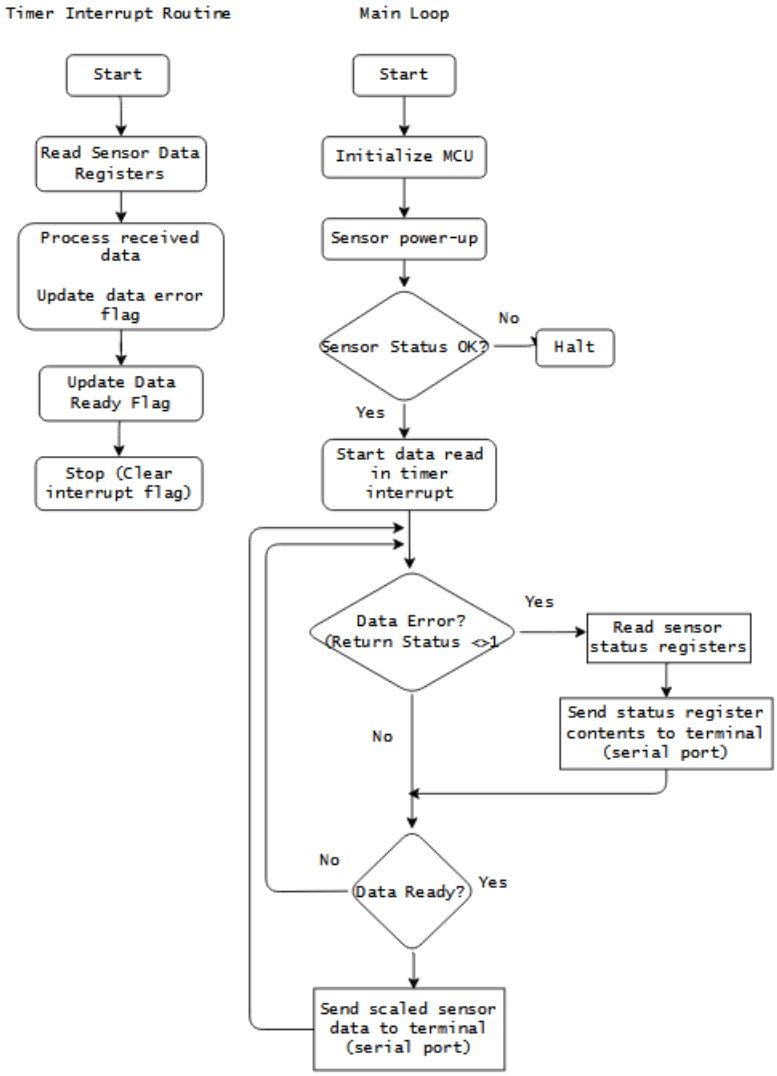

Figure 20 – General firmware flowchart

To collect the data from the sensor, a python script that reads the serial port of the computer is used, storing the data in a text file. Then, the data is pre-processed using Matlab to be analyzed in an Allan Variance algorithm in LabView. The result of the AVAR algorithm is then read into Matlab for data analysis and plot.

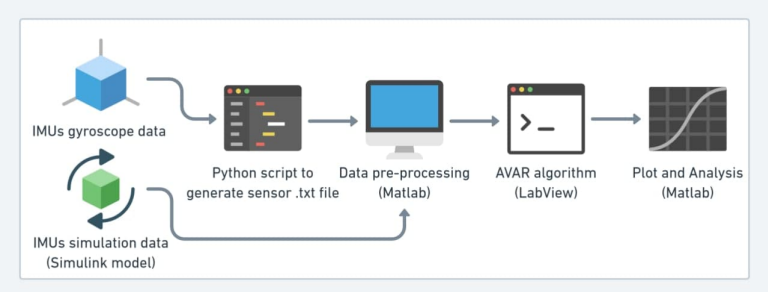

Figure 21 – General software flow

3.4.1 Generic gyroscope model in Simulink

This implementation of the model was the work of a research colleague, Victor Engers [7]. To represent all the sensors, an association of a generic single-axis gyroscope model was made (Figure 22), that contains the respective axis for each IMU, one for SCC2130, and three for BNO055 and MPU9250. After the concatenation, each vector is directed to output in this subsystem.

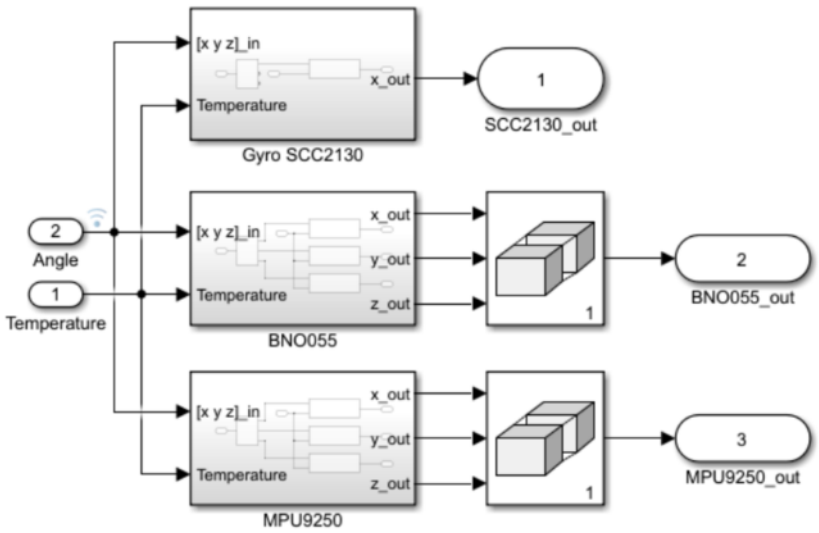

Figure 22 – System showing the model for each IMU, with its respective axis [7]

The model to represent a generic, single-axis gyroscope is shown in Figure 23. Since the noise analysis needs the sensor to be stationary, the input of the model, called real position, is zero and the output, measured position, is the value of gyroscope in angular velocity ($°/s$) to be analyzed. The rest of the model was divided into four parts each with a color.

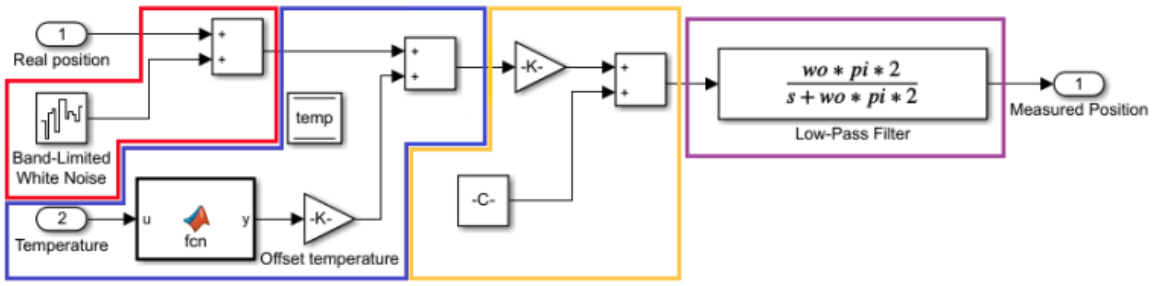

Figure 23 – Implemented model in Simulink representing a single-axis gyroscope [7]

In red, connected with a sum block with the input, is the part of the zero-mean Gaussian white noise (η_g). The block "Band-Limited White Noise" has two parameters, "Noise power" and "Sample time", the first can be found in datasheets as the Angle Random Walk and the second depends on the sensor acquisition time.

The blue part is where the temperature bias is added to the model. The function block is a script to receive the temperature input referencing the simulation time. The script receives the first temperature value in the data set, after this when there is a variation in the temperature, the signal value will change accordingly. After this block, the signal is multiplied by a gain block called "temperature sensitivity", as informed in datasheets.

In yellow, a gain block for all the previous system signals to allow a manual adjustment of the model. The other block is the constant bias block or offset, this block does not affect the Allan variance analysis, however, it is important to simulate the real sensor.

Lastly, in green, there is a first-order low-pass filter to attenuate the signal similarly to the utilized IMUs. The variable w_0 is the cut-frequency in *Hz* that is received by a parameter.

All the parameters for the model can be seen in Figure 24. After adjusting all the parameters, the output of the modeled sensor is saved in the output variable "Measured position".

	Parameters	ParameterGroupVar
#1	Offset Temperature	offset_temperature
#2	Offset Temperature Gain	offset_temp_gain
#3	Output Noise	output_noise
#4	Output Noise Gain	output_noise_gain
#5	System Gain	system_gain
#6	Static Bias	static_bias
#7	Cut Off Frequency (Hz)	wo
#8	Sample Frequency (Hz)	fs

Figure 24 – Gyroscope model parameters [7]

3.5 ALLAN VARIANCE METHODOLOGY TO EXTRACT THE NOISE TERMS

In an Allan Variance plot, there are certain key points to analyze the noise parameters, such as quantization noise, bias instability, angle random walk, and rate ramp, Figure 25 shows where to look for these parameters. For the bias instability, the Allan deviation plot reaches a minimum before increasing again, determining this point and then dividing the value by 0.664 , yielding a bias instability in *deg*/*h*.

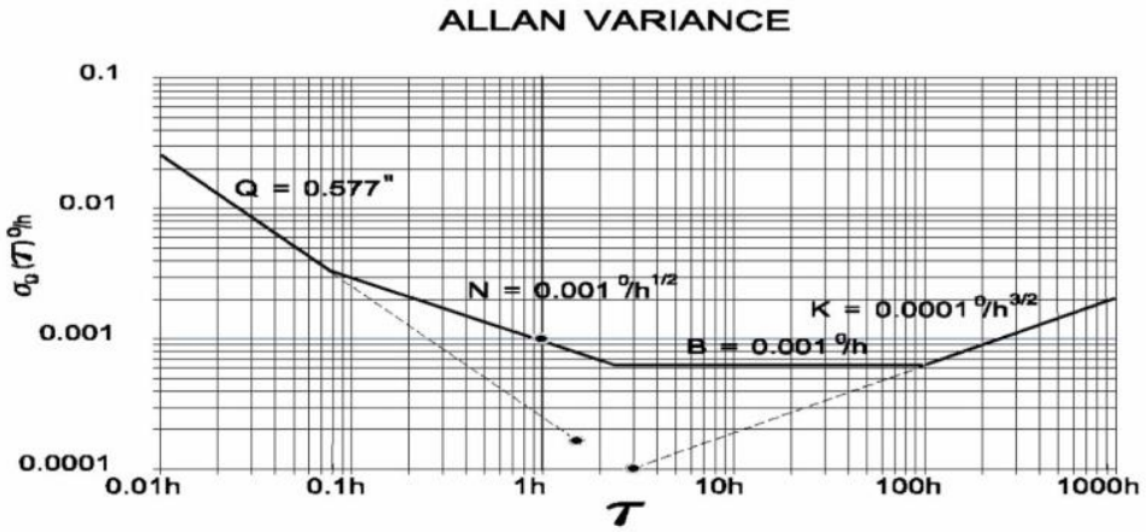

Figure 25 – Allan variance plot showing the calculation of the parameters [25]

The angle random walk (ARW) in an Allan deviation plot is the point where τ equals 1 hour, this method of obtaining the coefficient already extracts the value in $°/\sqrt{h}$ if the angular velocity data is also in hours. Another method of determining the ARW of an Allan plot in determining the Allan deviation is $\tau = 1s = 10^0$. Then, multiplying this value to 60 to get the angle random walk in $deg/\sqrt{hr}$. As an example, Figure 26 shows a plot of an allan deviation of some gyroscope, and equation 28 shows the conversion of units.

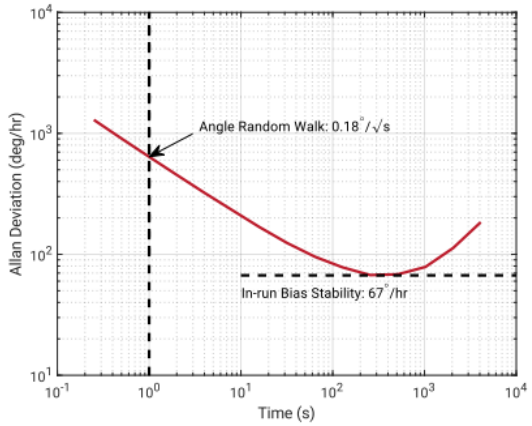

Figure 26 – Allan variance plot showing the calculation of the parameters [12]

$$ARW = \frac{0.18°}{s} * \frac{60s}{\sqrt{hr}}$$
$$ARW = \frac{10.8°}{\sqrt{hr}} \tag{28}$$

4 TEST AND RESULTS

4.1 INTRODUCTION

This chapter is devoted to demonstrating the results for data acquisition and the practical implementations of the AVAR method to characterize the different types of noises in the analyzed IMUs. As well as results for the gyroscope model analysis and combination of inertial sensors.

4.2 TEST ENVIRONMENT

Three different IMUs were involved in evaluating the use of Allan Variance in modeling gyroscope inertial sensor noise and the use of combined commercial sensors to boost their performance, all acquisitions were made with the sensor fully at rest.

- Dataset one: static test with the first version of the board running for 5 hours, with a sampling rate of 500 Hz in a closed room with ambient temperature.
- Dataset two: static test with the second version of the board running for 12 hours at 50 Hz sampling rate inside a thermal chamber set at a constant temperature of 26 degrees Celsius.
- Dataset three: static test with the second version of the board for 12 hours at 50 Hz sampling rate inside the thermal chamber set to a varying temperature.

The first test was executed at the beginning of the research, in the SpaceLab laboratory room at UFSC with ambient temperature, where the sensors SCC2130/2230, BNO055, and MPU9250 were evaluated, to characterize the noise levels of the gyroscopes, in addition to their bias instability. For the second and third tests, a thermal chamber (Figure 27) made available by the instrumentation and sensor laboratory at UNICAMP was used, where the BNO055 and SCC2130/2230 sensors were evaluated with different mechanical arrangements and a number of sensors on the first board. Two acquisitions were performed with different temperature profiles to characterize the noise levels of the sensors and their bias instability.

(a) Outside (b) Inside

Figure 27 – Thermal chamber

4.3 DATA ACQUISITION RESULTS

4.3.1 MPU9250

For the MPU9250 experiment, the acquisition was transferred at a rate of 500 Hz, following the MPU's datasheet [17] recommendation that the acquisition rate was higher than the sample rate of the sensor. These acquisitions were made in dataset one that used the first version of the Printed circuit board (PCB) in a room with ambient temperature and it was cut to 2.7 hours. The raw gyro result for the three-axis can be seen on Figure 28.

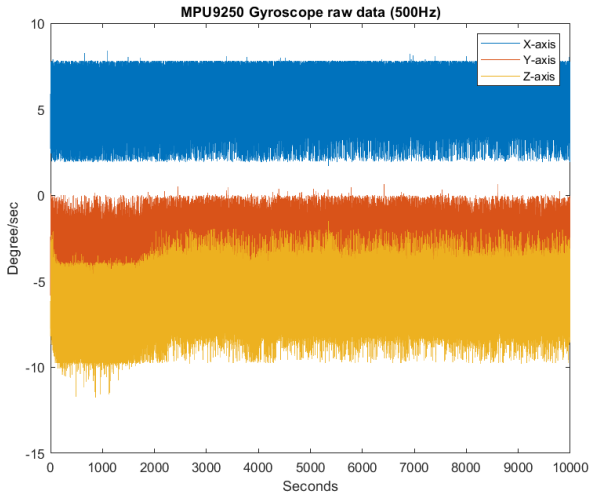

Figure 28 – MPU9250 3-axis gyroscope experiment data

The temperature plot for the dataset acquisition is shown in Figure 29. During the experiment, it remained practically constant, due to the room being with closed windows. The data points for the temperature will be used to create the sensor model.

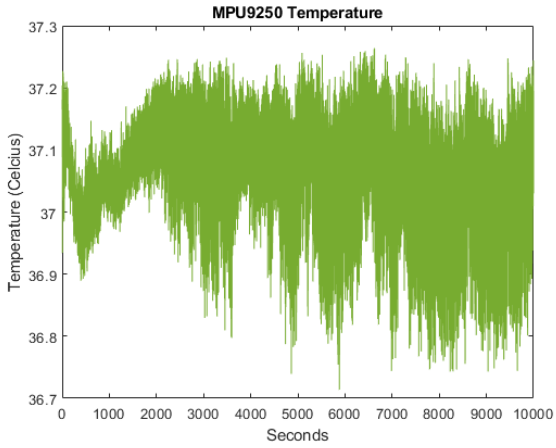

Figure 29 – MPU9250 experiment temperature

4.3.2 BNO055

The gyroscope data from the BNO055 for dataset two of the experiment is shown in Figure 30. In this data, there are 40000 seconds (11.1 hours) of acquisition time. For BNO 2, a cut-off was performed on the data to remove unwanted noise from the acquisition, leaving it at about 25000 seconds (6.9 hours).

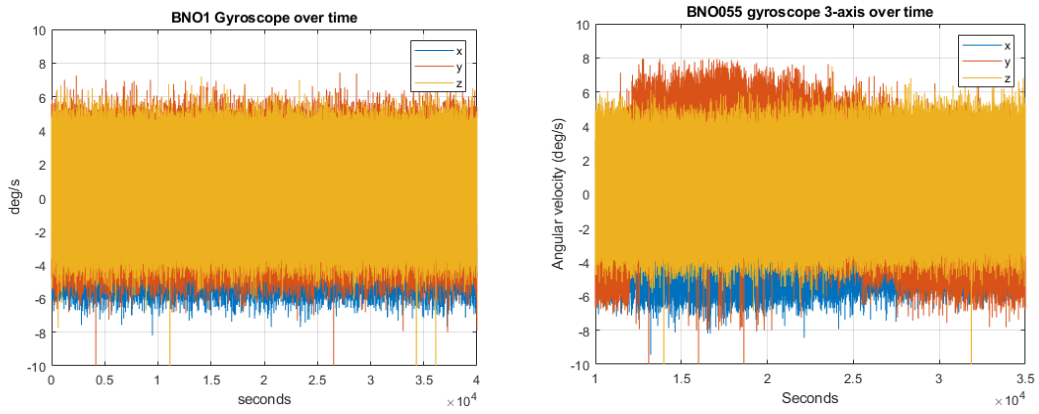

(a) Dataset 2 (b) Dataset 3

Figure 30 – BNO055 3-axis gyroscope experiment data in time

For this acquisition, a low-pass filter configured in the sensor is set at a frequency of 64 Hertz. Evaluating the data, the gyro axis behaviors were similar between the sensors.

The BNO's temperature is acquired using its internal sensor. It delivers only one byte of signed integer data which means that the value is always rounded to 1-degree Celsius. To have a better visualization of the plot, a moving average function was utilized. Figure 31shows dataset two and three acquisitions.

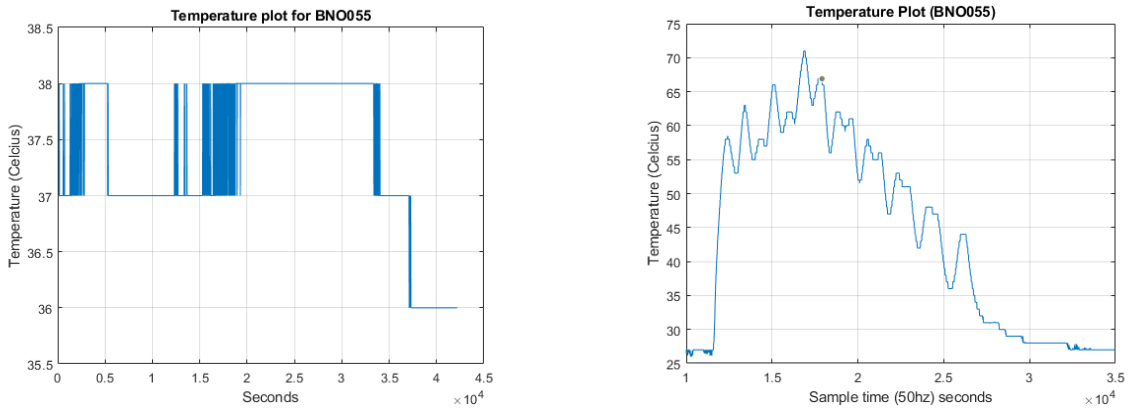

(a) Dataset 2 (b) Dataset 3

Figure 31 – Temperature plots for BNO055

4.3.3 SCC2130/2230

In the SCC2130/2230 experiment, three readings at different datasets were recorded. The first dataset occurred at a transfer rate of 500 hertz, the second and third at 50 hertz. Murata recommended a transfer rate of 2300 Hertz in his datasheet, but due to the size of the files and reading multiple sensors at the same time, these reduced sample times were chosen. The plots for the gyroscope in time are shown in Figure 32, dataset one corresponds to a 5-hour capture while dataset two and three corresponds 11.1 hours. Notice the dispersion of the values, even though the sensor was static the entire time.

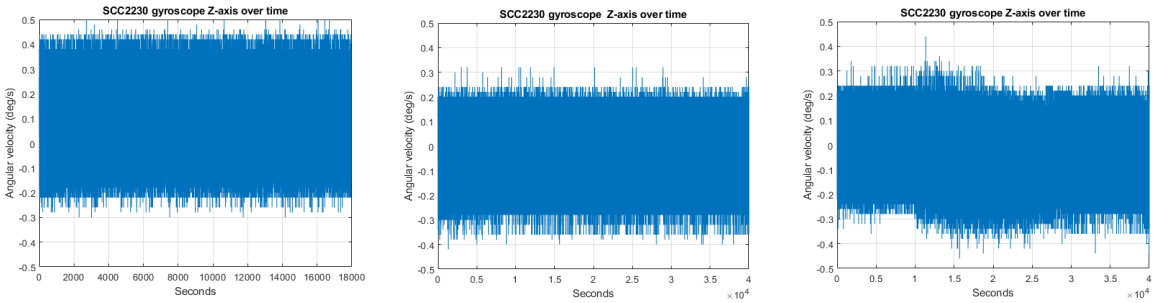

(a) Dataset 1 (b) Dataset 2 (c) Dataset 3

Figure 32 – SCC2130 X-axis gyroscope experiment data in time

The temperature plot for all datasets is illustrated in Figure 33. For datasets one and two, there is a small temperature variation during the acquisition, not exceeding one degree Celsius. In dataset three, a unique temperature variation was programmed in the chamber, in order to verify the outcome of a thermal noise in the sensor. These temperature data points will be used to create the sensor model.

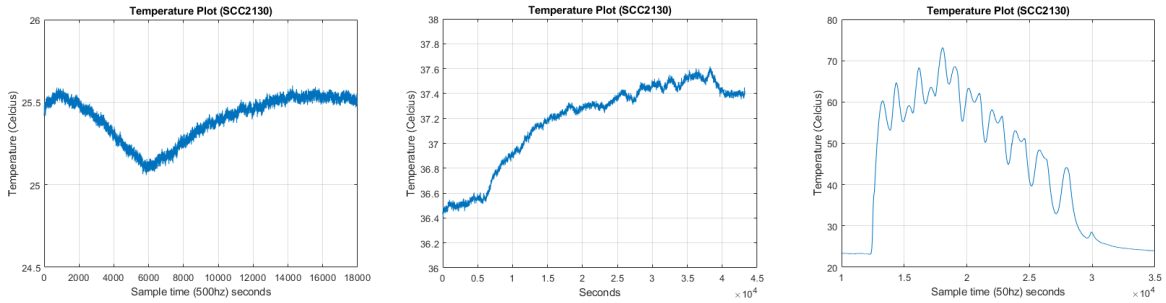

(a) Dataset 1 (b) Dataset 2 (c) Dataset 3

Figure 33 – Temperature plots for SCC2130/2230

4.3.3.1 Turn-on bias variation effect

An experiment to analyze the turn-on bias variation effect was conducted. A hundred quick acquisitions of less than 1 second of data for the SCC2130/2230 gyroscope were collected at 500Hz. With this data, two histograms were plotted in Figure 34 to observe the distribution of the angular motion.

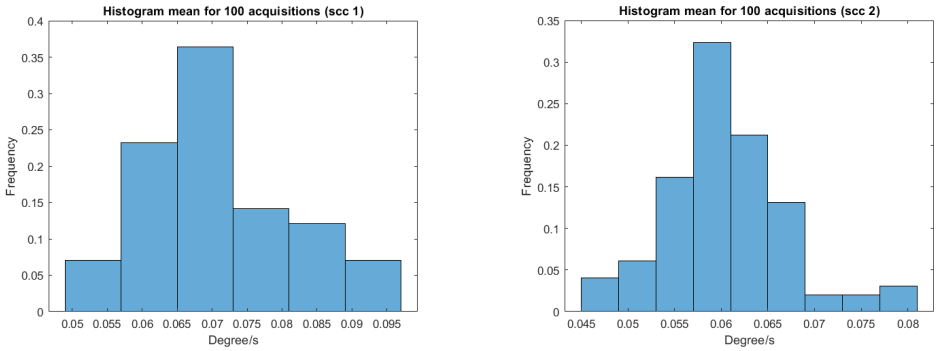

(a) Sensor 1 (SCC2230) (b) Sensor 2 (SCC2230)

Figure 34 – Histogram showing the frequency that values appear on a 100 acquisition data for the sensors

For the first sensor, the peak value was around 0.07°/*sec*, with values not well distributed. For the second sensor, we noticed more distributed values around the 0.06°/*sec* peak angular velocity. The experiment was investigative to evaluate the distribution of values when powering the sensor, checking its turn-on bias.

4.4 AVAR IMPLEMENTATION

The Allan Deviation (σ) characteristic curves were constructed under the LabView environment following the methodology and equations explained in Chapter 3. With these curves, it's possible to identify the error and noise terms affecting the sensors.

From the time domain of the datasets, the length of the dataset is shown as N. The firmware to obtain the data used a timer to guarantee the sample time, however, it is possible to also inspect this using the number of a sample τ_0 and timestamps provided by the sensors and then calculate the frequency f.

The average factor m value can be chosen arbitrarily fulfilling the condition $m < (N-1)/2$, a vector of log spaced numbers between 1 and $(N-1)/2$ is created. Therefore, the cluster time τ is a vector with logarithmically spaced values, with $\tau = m * \tau_0$. The computation of the AVAR in terms of averages of output samples over each cluster was done using equation 17, rewritten here.

$$\sigma^2(\tau) = \frac{1}{2\tau^2(N-2m)} \sum_{k=1}^{N-2m} (\theta_{k+2m} - 2\theta_{k+m} + \theta_k)^2, \tag{29}$$

where m is the averaging factor, $\tau = m * \tau_0$ is the averaging time, N is the total number of samples and k is a set of discrete values that varies from 1 to $N-2m$. The AVAR (σ^2) is calculated for each τ value. The Allan deviation (σ) is obtained applying a square root of the AVAR value.

The noises that oscillate frequently in the curves are located in the area with decreasing slopes because this section of the curve a has a short cluster time frame, therefore making it fluctuate in fewer samples. The noise that oscillates over longer time frames begins to impact larger groups of averaged data in the regions with rising slopes.

4.4.1 MPU9250 Allan Variance noise analysis

Two and a half hours were collected at room temperature (Figure 29). Applying the Allan variance method to the whole dataset one, a log-log plot of MPU9250 three-axis gyroscope Allan standard deviation in $°/h$ versus cluster time in seconds is shown in Figure 35.

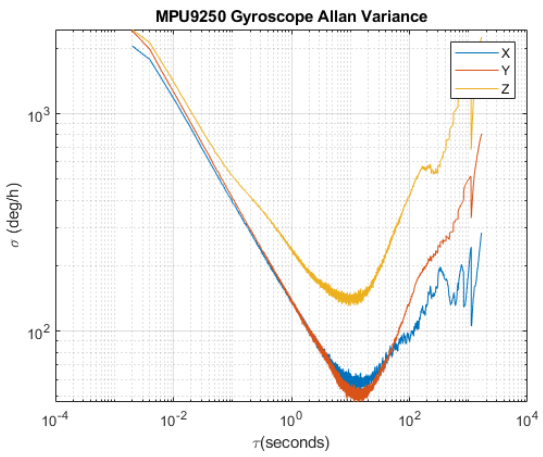

Figure 35 – MPU9250 Gyro Allan variance result

Analyzing the plot, a very similar curve can be seen for the X and Y axes, with very comparable ARW and BI parameters values. The Z-axis, on the other hand, has a noisier behavior. The values from the plot analysis are in the Table 5.

Dataset 1 (MPU9250)	**ARW**($°/\sqrt{h}$)	**BI**($°/h$)
Axis X	3.09	88.91
Axis Y	2.70	78.07
Axis Z	5.40	211.4

Table 5 – AVAR analysis parameter values for Figure 35

After characterizing the types and values of noises that affect the gyroscope using the AVAR method, the results for the X and Y-axis showed an expected behavior, while the Z-axis presented greater noise. The values obtained by Zheng et al. [32] can be compared with those obtained in this work since the authors used the same sensor. Therefore, we can conclude that the methodology employed in the AVAR method was successful in the verification of the noise parameters.

4.4.2 BNO055 Allan Variance analysis

For dataset two, 11.1 hours of static data were collected inside a thermal chamber programmed to a fixed temperature (Figure 31a). Applying the Allan variance method to the whole data set, a log-log plot of the four BNO055 sensors with the three-axis versus cluster time is shown in Figure 36.

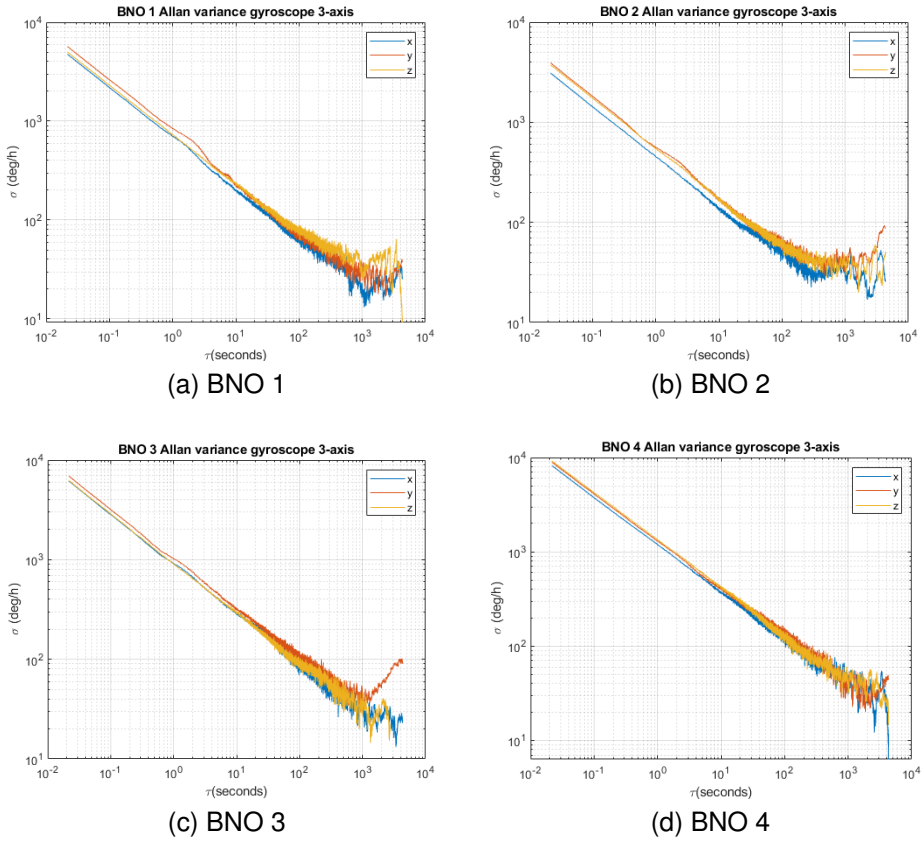

(a) BNO 1 (b) BNO 2

(c) BNO 3 (d) BNO 4

Figure 36 – Dataset 2 BNO055 Gyro Allan variance result for all axis

The sensors BNO 1 and BNO 3 are located on top of the board, while BNO 2 and BNO 4 are on the bottom. Analyzing the AVAR data, the Table 6 was built.

Dataset 2 (BNO 1)	**ARW**($°/\sqrt{h}$)	**BI**($°/h$)
Axis X	10.0	39.91
Axis Y	12.0	44.42
Axis Z	15.0	44.88
Dataset 2 (BNO 2)	**ARW**($°/\sqrt{h}$)	**BI**($°/h$)
Axis X	7.5	46.23
Axis Y	9.2	60.72
Axis Z	10.0	58.01
Dataset 2 (BNO 3)	**ARW**($°/\sqrt{h}$)	**BI**($°/h$)
Axis X	16.0	45.63
Axis Y	18.5	66.68
Axis Z	17.0	50.25
Dataset 2 (BNO 4)	**ARW**($°/\sqrt{h}$)	**BI**($°/h$)
Axis X	18.0	51.82
Axis Y	21.0	46.91
Axis Z	23.0	56.38

Table 6 – AVAR analysis parameter values for Figure 36

The results obtained in the characterization of the types and noise values of

the sensors of the second dataset at constant temperature were satisfactory, with similar behavior between the axes. The four sensors have similar graphical behavior, the noisiest being BNO 4. In the work of Venek et al. [29], the authors used the same sensor and obtained parameters values, with 7.95°/*h* of BI and 2.73°/$\sqrt{h}$ of ARW. This disparity may be due to the lower transmission rate used in this work (50 Hz), or optimizations applied in the firmware.

For dataset three, about 25000 seconds (6.9 hours) of static data were collected inside a thermal chamber in a varying temperature profile, first heating up then cooling it down (Figure 31b). Applying the Allan variance method to the whole data set, a log-log plot of the four BNO055 sensors with the three-axis versus cluster time is shown in Figure 37.

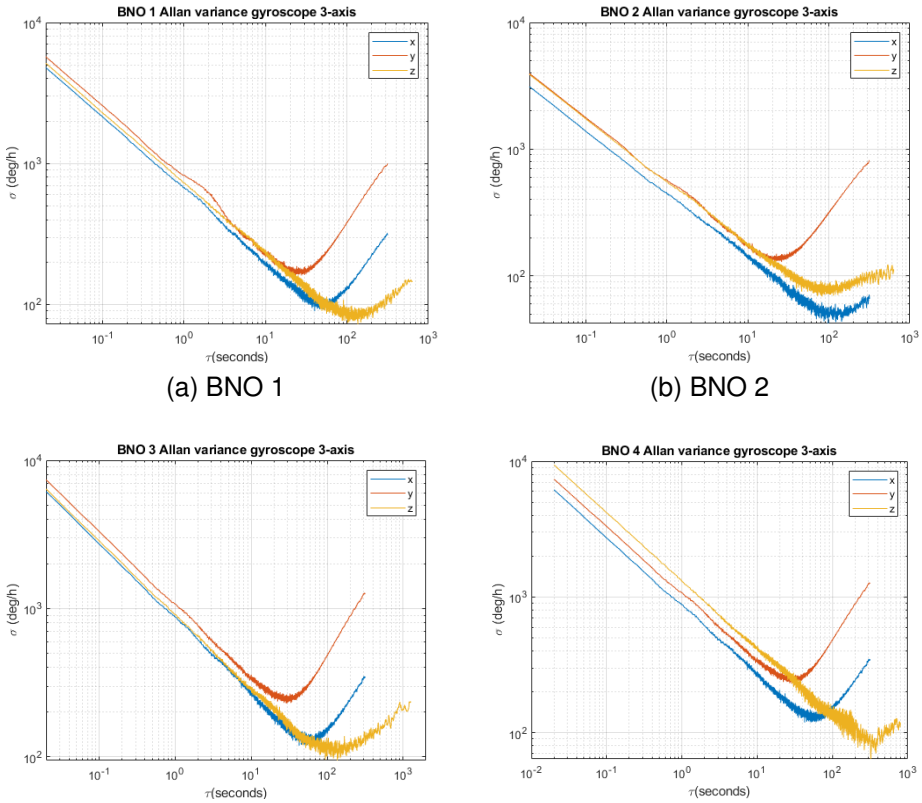

(a) BNO 1 (b) BNO 2

(c) BNO 3 (d) BNO 4

Figure 37 – Dataset 3 BNO055 Gyro Allan variance result for all axis

This acquisition purposely used a brusque temperature variation to evaluate the influence of thermal noise for data acquisition in gyroscopes. Table 7 shows the values for the noise parameters.

Dataset 3 (BNO 1)	**ARW**($°/\sqrt{h}$)	**BI**($°/h$)
Axis X	10.20	153.43
Axis Y	10.30	258.61
Axis Z	10.40	126.86
Dataset 3 (BNO 2)	**ARW**($°/\sqrt{h}$)	**BI**($°/h$)
Axis X	7.50	77.05
Axis Y	10.0	209.28
Axis Z	10.0	118.73
Dataset 3 (BNO 3)	**ARW**($°/\sqrt{h}$)	**BI**($°/h$)
Axis X	10.5	195.72
Axis Y	10.8	370.30
Axis Z	11.0	169.70
Dataset 3 (BNO 4)	**ARW**($°/\sqrt{h}$)	**BI**($°/h$)
Axis X	10.50	198.43
Axis Y	11.0	381.14
Axis Z	11.20	130.66

Table 7 – AVAR analysis parameters values for Figure 37

The results obtained for dataset three, which was subjected to temperature variation, denote that the ARW parameters was stable for the sensors, while the BI presented a discrepant behavior between the axes. Compared with dataset two, the BI values increased considerably. For the BNO 1 sensor in the X-axis the BI value was 39.91 $°/h$ (Table 6), while for the same sensor in this analysis, the BI value increased to 153.43 $°/h$ (Table 7). This may be due to the sudden change in temperature submitted to the sensor, which was from 20 degrees Celsius to 70 degrees Celsius, shown in Figure 31b. This clearly indicates the need to include two separate parameters for BI in the model in the future: BI and thermal BI.

4.4.3 SCC2130/2230 Allan variance analysis

For dataset one, five-hour static data from SCC2230 were collected at room temperature (Figure 33a). Applying the Allan variance method to the whole data set, a log-log plot of gyroscope standard deviation versus cluster time is shown in Figure 38 for the first and second sensor.

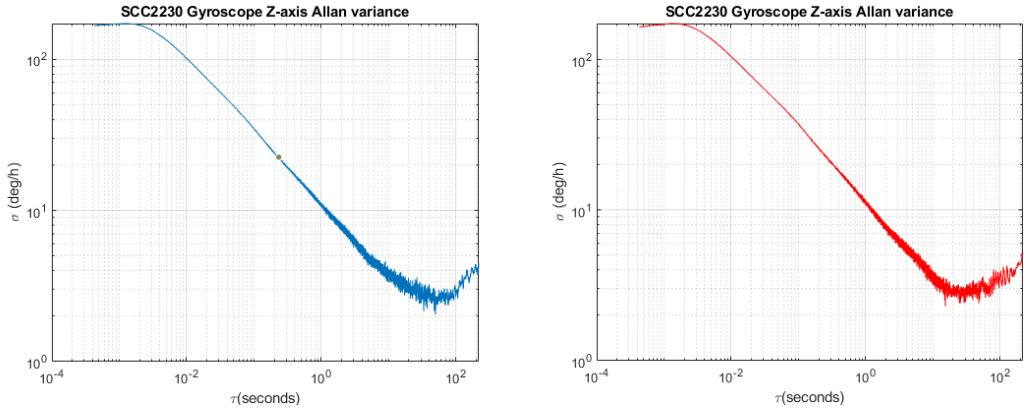

(a) SCC 1 (b) SCC 2

Figure 38 – Dataset 1 SCC2230 gyroscope Allan variance result for Z-axis

The SCC1 was located at the top of the PCB, while SCC 2 was at the bottom. The results of the analysis are in Table 8. Both gyroscopes in this analysis had low noise, with very similar BI and ARW parameters.

Dataset 1 (SCC 1)	**ARW**($°/\sqrt{h}$)	**BI**($°/h$)
Axis Z	0.20	4.11
Dataset 1 (SCC 2)	**ARW**($°/\sqrt{h}$)	**BI**($°/h$)
Axis Z	0.18	4.30

Table 8 – AVAR analysis parameters values for Figure 38

For these results, the plots presented similar behavior, indicating that the collected data are reliable. In the literature, few studies use the Allan variance (AVAR) method to analyze the noise of this sensor, however, the sensor datasheet [3] presents a noise analysis, which can be used for comparative purposes.

For dataset two, 11.1 hours of static data from SCC2130/2230 were collected at a fixed temperature inside the thermal chamber (Figure 33b). Applying the AVAR method to the whole data set, a log-log plot of the SCC2130/2230 Z and X-axis gyroscope standard deviation versus cluster time is shown in Figure 39 for all five sensors.

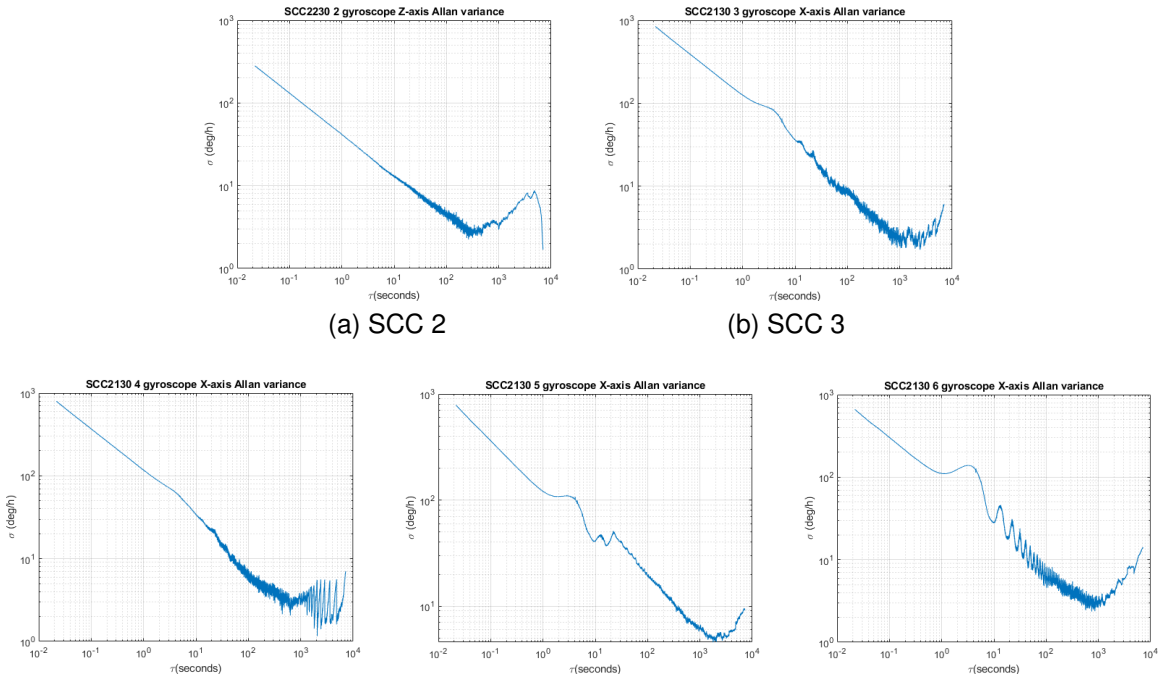

(a) SCC 2 (b) SCC 3

(c) SCC 4 (d) SCC 5 (e) SCC 6

Figure 39 – Dataset 2 SCC2130/2230 gyroscope Allan variance result for X/Z axis

For this dataset, the second version of the board was used, which contains six SCCs IMUs, however, one of them presented electrical problems and we could not capture its signal. Therefore, only five sensors were evaluated, two on top (SCC 3 and SCC 5) and three below (SCC 2, SCC 4, and SCC 6). The results for the AVAR parameters are in Table 9.

Dataset 2 (SCC 2)	**ARW**($°/\sqrt{h}$)	**BI**($°/h$)
Axis Z	0.68	4.15
Dataset 2 (SCC 3)	**ARW**($°/\sqrt{h}$)	**BI**($°/h$)
Axis X	1.10	3.63
Dataset 2 (SCC 4)	**ARW**($°/\sqrt{h}$)	**BI**($°/h$)
Axis X	1.50	4.44
Dataset 2 (SCC 5)	**ARW**($°/\sqrt{h}$)	**BI**($°/h$)
Axis X	3.10	7.64
Dataset 2 (SCC 6)	**ARW**($°/\sqrt{h}$)	**BI**($°/h$)
Axis X	1.40	4.54

Table 9 – AVAR analysis parameters values for Figure 39

Observing the data in Table 9, SCC 2 had a small increase in ARW compared to SCC 2 from the previous dataset, which may have been caused by the lower acquisition rate. SCC 3, 4, and 6 had similar parameters, while SCC 5 may have suffered from some problem with its acquisition, as its parameter was about two times higher. Analyzing the

behavior of the graph, it can be seen that SCC 5 and 6 may have a problem, while SCC 3 and 4 are quite similar and SCC 2 had a similar result from the previous dataset.

For dataset three, about 25000 seconds (6.9 hours) of static data were collected inside a thermal chamber in a varying temperature profile (Figure 33c). Applying the Allan variance method to the whole data set, a log-log plot of the five SCC2130/2230 sensors with the three-axis versus cluster time is shown in Figure 40.

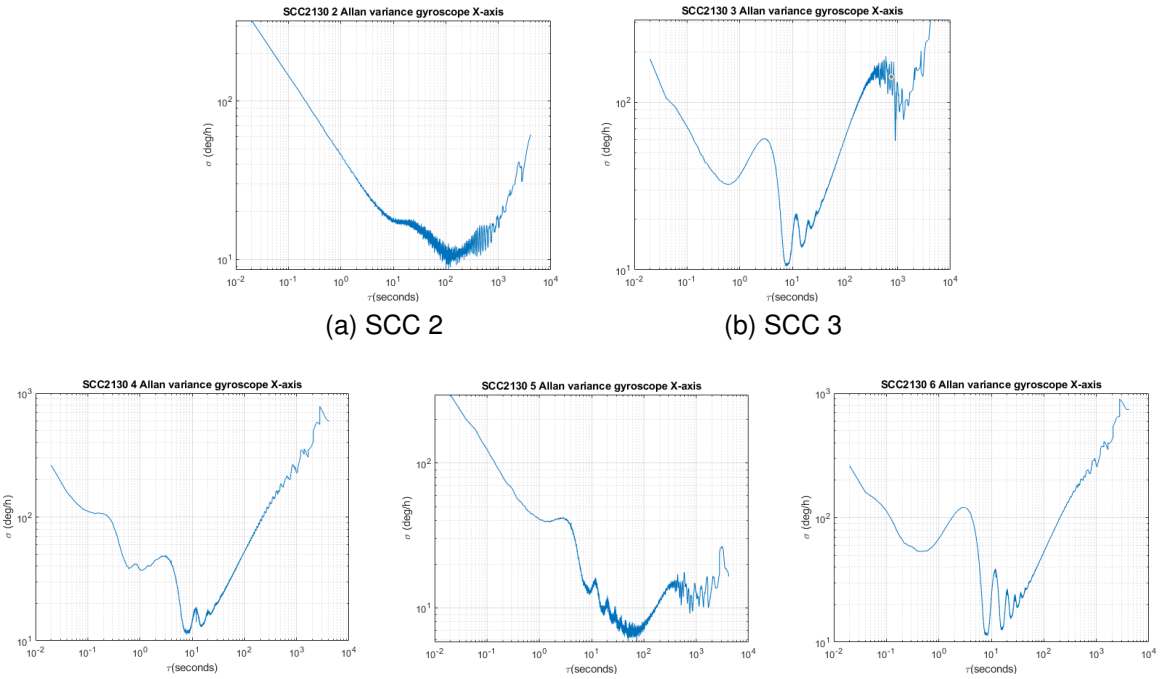

(a) SCC 2 (b) SCC 3

(c) SCC 4 (d) SCC 5 (e) SCC 6

Figure 40 – Dataset 3 SCC2130/2230 gyroscope Allan variance result

Analyzing Figure 40, only SCC 2 obtained an AVAR where it is possible to extract the parameters, with ARW of $0.7 degree/\sqrt{h}$ and BI of 16 $degree/h$. Similar to what was observed with dataset two for this sensor, because of the sharp temperature variation, the BI value was much higher, which again indicates the need to separate the different BI noise sources in the generic model. The other sensors behaved uncharacteristically in this test, and it wasn't possible to extract the noise parameters.

4.5 MODEL RESULTS

An Allan variance curve is defined by several parameters, among which two are relevant to the suggested mathematical model: the ARW and BI. The angle random walk results from noise present in angular velocity measurements, which produces a random walk when integrated in time to compute the rotation angle. The bias instability results from the presence of correlated noise in the gyroscope, which changes the bias randomly in time [28].

These parameters were used after the analysis in section 4.4 to create a simulated gyroscope with the Simulink model. Currently, it only supports the bias instability parameter that is an electronic originated bias, captured with stable temperature.

4.5.1 MPU9250

The noise settings listed in Table 5 were used in the MPU9250 axis configuration block (notice that the values are in seconds), as illustrated in Figure 41. To demonstrate a higher resemblance between the real and simulated data, a cut-off frequency of 120Hz was chosen instead of the 188Hz configured on the MPU9250.

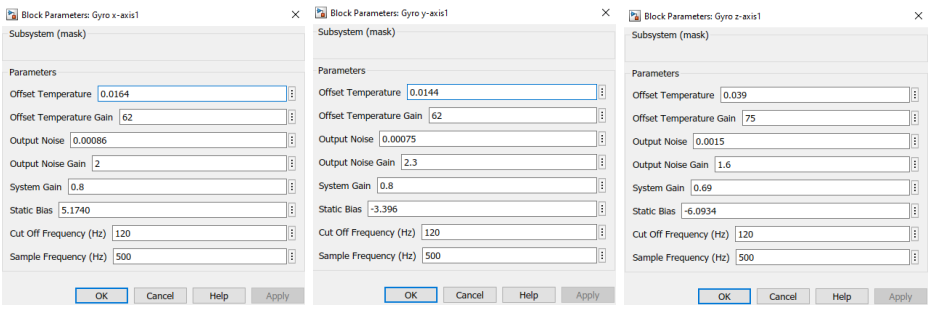

Figure 41 – Configuration blocks for the MPU9250 axis

The simulation time of the model is 10,000 seconds (2.7 hours) in 500 Hz, the same time as the real data acquisition. Figure 42 shows the comparison between the model with the actual data results after applying the AVAR.

The model behaved as expected for a short cluster time, as projected for the ARW and BI parameters. For longer times, the behavior differed because the model had no requirement to simulate noise parameters that appear at longer times, such as the rate random walk. To obtain this result, the model gain was adjusted as presented in Figure 41.

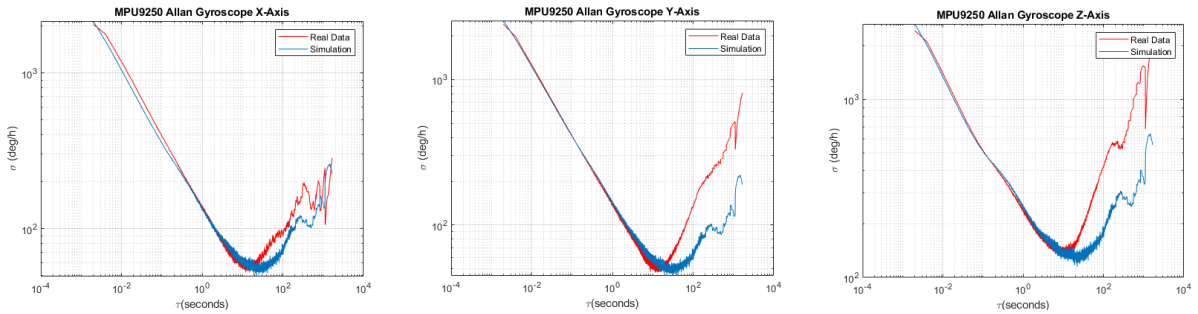

(a) X-Axis (b) Y-Axis (c) Z-Axis

Figure 42 – MPU9250 Gyro Allan variance result for the model, comparing with the real data results

Finally, a comparison of the Allan variance of the acquisition and a simulation with the values provided by the datasheet of the MPU9250 [17] was also done and the result can be seen in Figure 43. The simulation with the datasheet values is found to be sufficiently close to the axis values obtained from the sensor, and even consistent with the dynamic drift of the z-axis. The ripple in the negative slope of the AVAR from the datasheet shows a strong influence of the temperature on the simulated data, possibly even indicating a noisy and unrealistic acquisition of the temperature values.

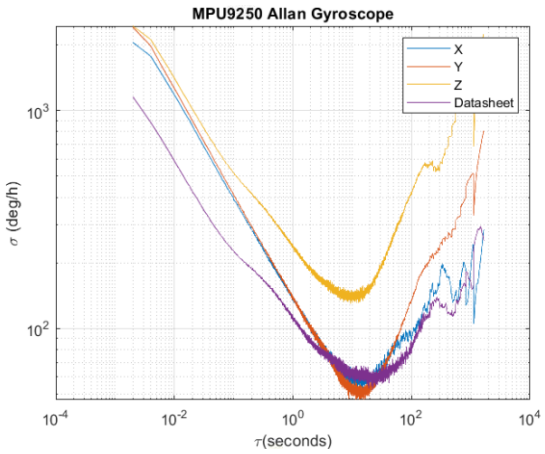

Figure 43 – Comparison of AVAR from acquisition (all axis) and datasheet (x-axis)

4.5.2 BNO055

The parameters of the second sensor, called BNO 2 on the Allan variance analysis in Table 6 were used for the configuration block of the model for the BNO055, the values are related to seconds instead of hours and can be seen in Figure 44. The cut-off frequency for the digital filter is 64 Hz.

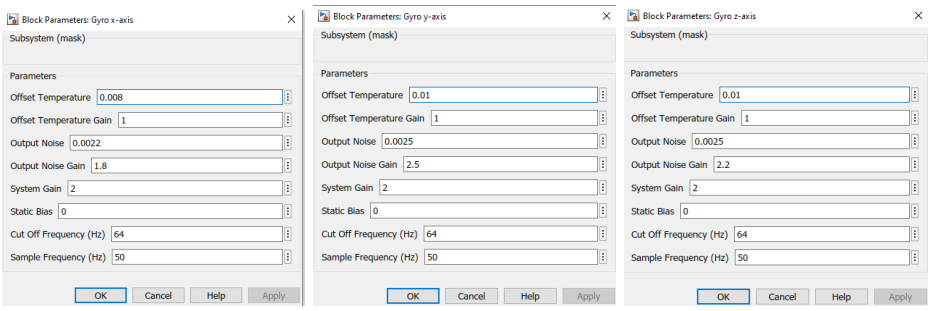

Figure 44 – Configuration blocks for the BNO055 axis

The simulation time was 28000 seconds (7.7 hours) in 50 Hertz. Figure 45 shows the comparison of Allan's analysis of the model with the real data for each axis.

The plots of the BNO sensor presented similar noise behavior to the real data, after the adjustment of the model gains as shown in Figure 44. In the same way as observed for the MPU9250 sensor, the model adjusted for short cluster time.

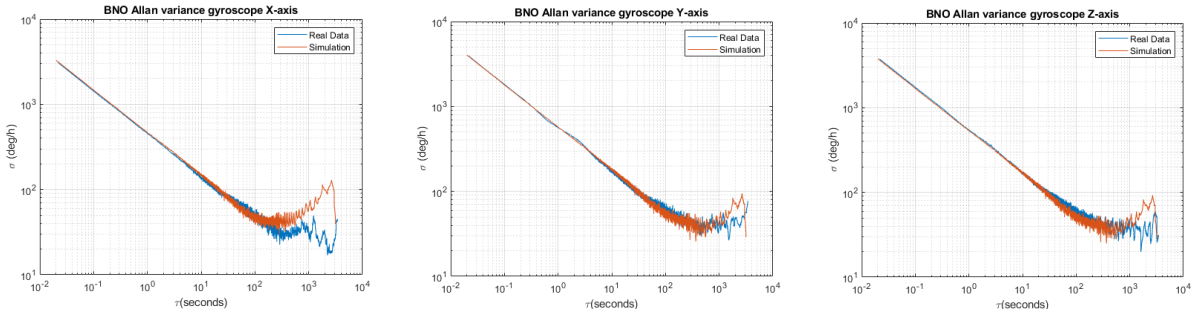

(a) X-Axis (b) Y-Axis (c) Z-Axis

Figure 45 – BNO055 gyroscope Allan variance result for the model, comparing with the real data results

A comparison between the Allan variance and a simulation with the values provided by the BNO's datasheet [13] was done and the result can be seen in Figure 46. Observing the simulation plot, it is noted that the bias instability and angle random walk parameters provided by the datasheet are smaller, possibly because of the use of ideal sensor parameters from the manufacturer.

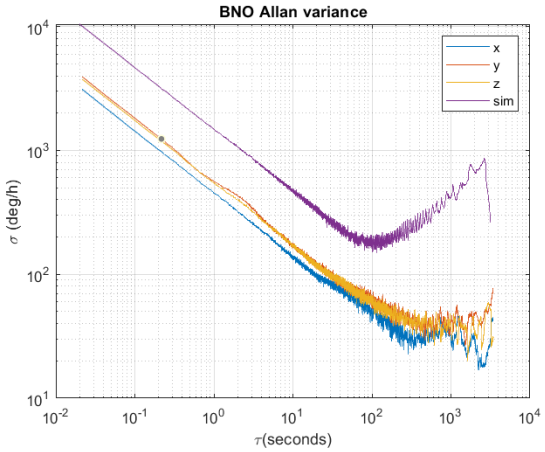

Figure 46 – Comparison of AVAR from acquisition (all axis) and datasheet parameters

4.5.3 SCC2130/2230

The parameters of the first dataset on Table 8 were utilized in the configuration block for the SCC2130/2230 X-axis, noting that the values are in seconds instead of hours and can be seen on Figure 47. The cut-off frequency is set to 60hz because the sensor internal filter that was configured on startup on this frequency.

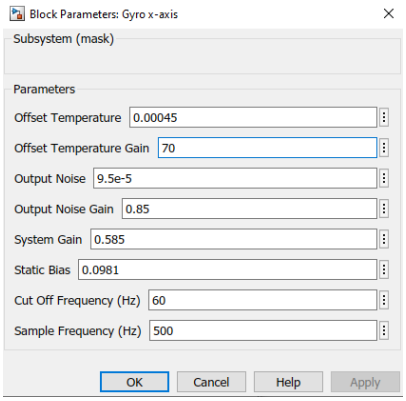

Figure 47 – Configuration blocks for the SCC2130 X-axis

The gyroscope simulation time was 18000 seconds (5 hours) in 500 Hertz. To analyze the simulated data, the Allan variance was computed and compared to the real data, showed in Figure 48.

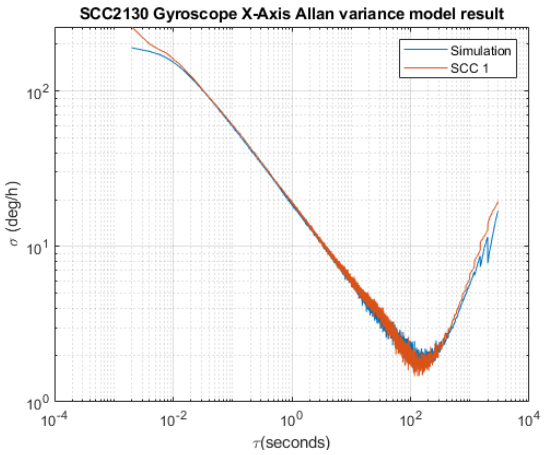

Figure 48 – SCC2130 Gyroscope Allan variance result for the model, comparing with the real data results

A great similarity between the two curves is observed, the model data adjusted to longer cluster times, even though the model was developed for shorter cluster times, taking into account the ARW and BI noise parameters. Such similarity at longer times can be considered random. To obtain this plot, an adjustment of the gains in the model was performed, as shown in Figure 47.

A simulation using the noise parameters given in the datasheet was also made, which can be seen in Table 10. The parameter values were taken from the datasheet's AVAR in Figure 49.

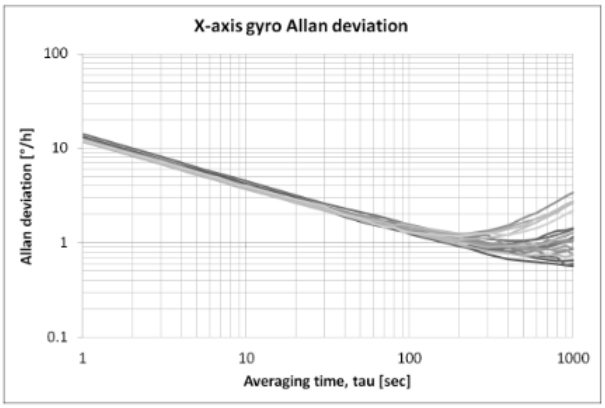

Figure 49 – SCC2130 Gyroscope datasheet Allan variance [3]

Datasheet	**ARW**($°/\sqrt{h}$)	**BI**($°/h$)
Axis X	0.17	1.47

Table 10 – AVAR values for the SCC2130 datasheet

Figure 49 shows a comparison between experimental, simulated, and datasheets values. The difference among the plots is due to lower bias instability of the data with a similar angle random walk.

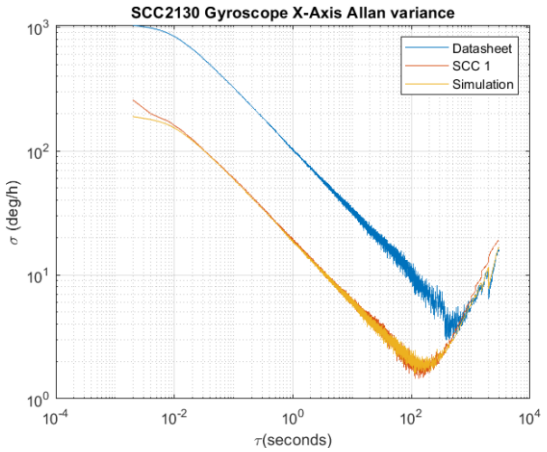

Figure 50 – Comparison of AVAR from acquisition, simulation and datasheet

4.6 IMU COMBINATION

This experiment consisted in combining the data from the gyroscopes to verify in practice whether it is possible to reduce the noise parameters of low-cost sensors using the mechanical arrangement to perform the offset compensation. The dataset is combined using a mean of the difference of the values point by point. Figure 51 illustrates the position of the sensors. Using this approach, it is expected a gain of $1/\sqrt{2}$ for the ARW values.

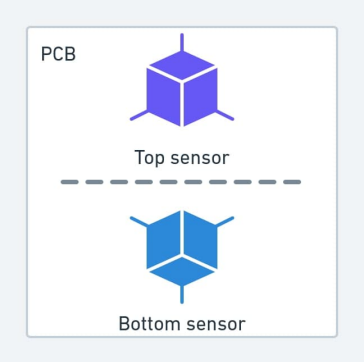

Figure 51 – Illustration to represent the position of the sensors in relation to the board

The combinations of inertial measurements to form a single measurement works if the IMUs are rigidly linked together, with a computational cost that depends on the number of IMUs. Skog et al. [23], by using a set of low-cost IMUs they concluded that this combination approach is feasible to improve the performance of the system. However, according to the authors, using the weighted mean instead of the arithmetic mean can improve the system's performance.

4.6.1 BNO055 combination

Dataset two was used to perform the combination of data for BNO055's gyroscope, and the result for the Allan plot is shown in Figure 52. The parameters values for the difference are shown in Table 11.

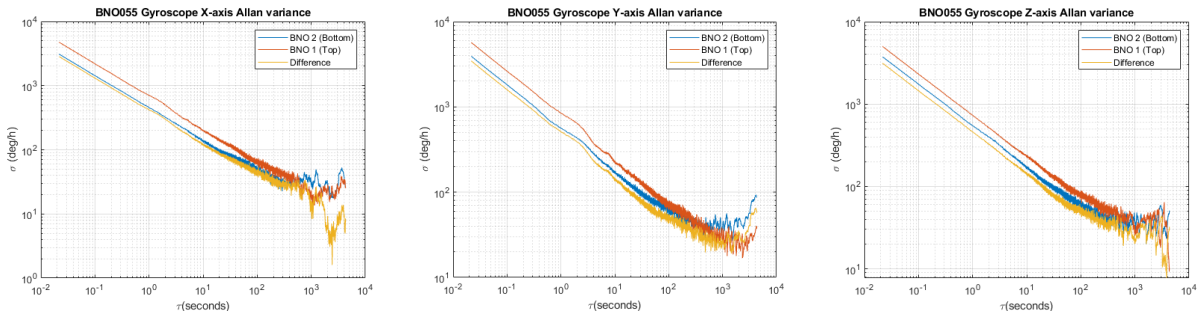

(a) X-Axis (b) Y-Axis (c) Z-Axis

Figure 52 – Dataset 2 BNO055 gyroscope for all axis Alan variance

Dataset 2 (BNO 1)	**ARW**($°/\sqrt{h}$)	**BI**($°/h$)
Axis X	10.0	39.91
Axis Y	12.0	44.42
Axis Z	15.0	44.88
Dataset 2 (BNO 2)	**ARW**($°/\sqrt{h}$)	**BI**($°/h$)
Axis X	7.5	46.23
Axis Y	9.2	60.72
Axis Z	10.0	58.01
Dataset 2 (Difference)	**ARW**($°/\sqrt{h}$)	**BI**($°/h$)
Axis X	6.5	36.74
Axis Y	7.5	41.50
Axis Z	7.2	42.62

Table 11 – AVAR analysis parameters values for Figure 52

A combination of sensors in a different mechanical arrangement of the PCB was performed, with the BNO 1 sensor located on the top of the board and the BNO2 sensor below. Analyzing the yellow curve, which is the difference between the sensors (Figure 52), one can see a reduction in the noise parameters analyzed, which indicates that this combination was effective in increasing the performance of the sensor.

4.6.2 SCC2230 combination

For the SCC2230 gyroscope, dataset one was used to perform the combination of data, and the result for the Allan plot is shown in Figure 53. The parameters values for the difference are shown in Table 12.

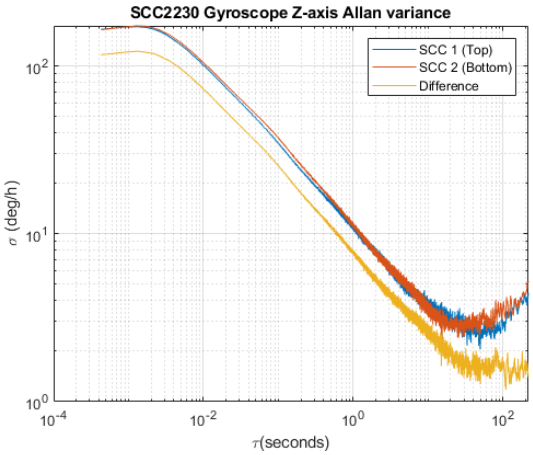

Figure 53 – Dataset 1 2230 gyroscope Allan variance data combination

Dataset 1 (SCC 1)	**ARW**($°/\sqrt{h}$)	**BI**($°/h$)
Axis Z	0.2	4.11
Dataset 1 (SCC 2)	**ARW**($°/\sqrt{h}$)	**BI**($°/h$)
Axis Z	0.18	4.30
Dataset 1 (Difference)	**ARW**($°/\sqrt{h}$)	**BI**($°/h$)
Axis Z	0.13	2.32

Table 12 – AVAR analysis parameters values for for Figure 53

This experiment was performed by combining two SCC2230 sensors, one located on top of the PCB and the other below. By analyzing the yellow curve (Figure 53), a reduction in the noise factors is evident compared to the data obtained by the sensors. Looking at the ARW data in Table 12 it can be seen that there was an approximate gain of $1/\sqrt{2}$. For the SCC 2 sensor, the ARW was $0.18°/\sqrt{h}$, by performing the $1/\sqrt{2}$ gain on this value, the ARW would be $0.127°/\sqrt{h}$, very close to the measured value for the difference value.

5 CONCLUSION

The work developed used different areas of knowledge to achieve results in the field of embedded inertial navigation. Initially, a study was conducted on the quantization of noise components in gyroscopes integrated into inertial measurement units, and the operation of gyroscopes, which enabled the development of a generic model for simulating gyroscope data, which can be replicated for various types of gyroscopes, by setting the desired parameters. In addition, part of the work was dedicated to the development of firmware for sensor acquisition, implementation of algorithms for calculating Allan's variance, and development of printed circuit boards with IMU.

From the three commercial-grade sensor models with different price ranges, ranging from tens to hundreds of dollars, three sets of experimental data were acquired. The acquisition took place with the static sensors under the following conditions: the first in a closed room at the university at room temperature, the second using a thermal chamber at a constant temperature, and the third using a thermal chamber at variable temperature. From these experimental data, the noise parameters were analyzed using the Allan variance to use the results to validate the generic model implemented in Simulink. In the end, a combination of data from gyroscopes of the same model in different mechanical arrangements was performed, where improvements in the system performance were observed.

The general objectives of the work were achieved as we describe in chapter 5, especially with the characterization of experimental noise factors in low-cost IMUs, as well as the implementation of the mathematical model for the noise parameters for each of the IMUs. The model used successfully reproduced the gyroscope data, achieving a behavior similar to the real one. The data for the association of inertial units was also satisfactory, reducing the ARW noise level by a gain of $1/\sqrt{2}$, as expected.

5.1 FUTURE WORKS

During the development of this work the following possibilities of future work have been identified:

- The model can be improved by separating the bias noise of electronic and thermal origin so that it will will be possible to generate gyroscope data similar to gyroscopes in real applications.
- Apply data fusion techniques and evaluate more complex combinations of gyroscopes to reduce the Allan variance noise parameters.

BIBLIOGRAPHY

[1] David W Allan. “Statistics of atomic frequency standards”. *In*: *Proceedings of the IEEE* 54.2 (1966), pp. 221–230.

[2] Jared B Bancroft and Gérard Lachapelle. “Data fusion algorithms for multiple inertial measurement units”. *In*: *Sensors* 11.7 (2011), pp. 6771–6798.

[3] *Combined gyroscope and 3-axis accelerometer with digital SPI interface*. SCC2130. Murata Electronics. 2013. Available from: https://www.murata.com/~/media/webrenewal/products/sensor/pdf/datasheet/datasheet_scc2130-d08.ashx?la=zh-cn.

[4] Timothy P Crain, Robert H Bishop, and Tye Brady. “Shifting the inertial navigation paradigm with MEMS technology”. *In*: *Advances in the Astronautical Sciences* 137.25 (2010), p. 2010.

[5] John Weston David Titterton. *Strapdown Inertial Navigation Technology (IEE Radar, Sonar, Navigation and Avionics Series)*. 2nd ed. The Institution of Engineering and Technology, 2005.

[6] *EK-TM4C123GXL*. Available from: https://www.ti.com/tool/EK-TM4C123GXL.

[7] Vitor Diego Dias Engers *et al.* “Modelagem de ruidos de giroscopios MEMS comerciais para aplicações em navegação inercial”. *In*: (2021).

[8] Last Minute Engineers. *In-Depth: Interface MPU6050 Accelerometer and Gyroscope Sensor*. Dec. 2020. Available from: https://lastminuteengineers.com/mpu6050-accel-gyro-arduino-tutorial/.

[9] H. Hou and Naser El-Sheimy. “Inertial sensors errors modeling using Allan variance”. *In*: *Proc. ION GPS/GNSS* (Jan. 2003), pp. 2860–2867.

[10] “IEEE Standard Definitions of Physical Quantities for Fundamental Frequency and Time Metrology—Random Instabilities”. *In*: *IEEE Std Std 1139-2008* (2009), pp. c1–35. DOI: 10.1109/IEEESTD.2008.4797525.

[11] “IEEE Standard Specification Format Guide and Test Procedure for Single-Axis Interferometric Fiber Optic Gyros”. *In*: *IEEE Std 952-1997* (1998), pp. 1–84. DOI: 10.1109/IEEESTD.1998.86153.

[12] *Inertial Navigation Primer*. Available from: https://www.vectornav.com/resources/inertial-navigation-primer.

[13] *Intelligent 9-axis absolute orientation sensor*. BNO055. Bosch Sensortec. 2014. Available from: https://cdn-shop.adafruit.com/datasheets/BST_BNO055_DS000_12.pdf.

[14] Quang Lam *et al.* "Gyro modeling and estimation of its random noise sources". *In*: *AIAA guidance, navigation, and control conference and exhibit*. 2003, p. 5562.

[15] ZL Mao. "Magnetic Field Measurement". *In*: *Atomic energy Press* (1985).

[16] Francesco Dell Olio Mario N. Armenise Caterina Ciminelli and Vittorio M. N. Passaro. *Advances in Gyroscope Technologies*. 1st ed. Springer, 2011.

[17] *MPU-9250 Product Specification Revision 1.1*. MPU-9250. Invensense Inc. 2015. Available from: https://invensense.tdk.com/wp-content/uploads/2015/02/PS-MPU-9250A-01-v1.1.pdf.

[18] Lawrence C Ng. *On the application of Allan variance method for ring laser gyro performance characterization*. Tech. rep. Lawrence Livermore National Lab., CA (United States), 1993.

[19] John-Olof Nilsson and Isaac Skog. "Inertial sensor arrays—A literature review". *In*: *2016 European Navigation Conference (ENC)*. IEEE. 2016, pp. 1–10.

[20] Athanasios Papoulis and S Unnikrishna Pillai. *Probability, random variables, and stochastic processes*. Tata McGraw-Hill Education, 2002.

[21] Michael Perlmutter and Laurent Robin. "High-performance, low cost inertial MEMS: A market in motion!" *In*: *Proceedings of the 2012 IEEE/ION Position, Location and Navigation Symposium*. IEEE. 2012, pp. 225–229.

[22] Derek K. Shaeffer. "MEMS inertial sensors: A tutorial overview". *In*: *IEEE Communications Magazine* 51.4 (2013), pp. 100–109. DOI: 10.1109/MCOM.2013.6495768.

[23] Isaac Skog, John-Olof Nilsson, and Peter Händel. "Pedestrian tracking using an IMU array". *In*: *2014 IEEE International Conference on Electronics, Computing and Communication Technologies (CONECCT)*. IEEE. 2014, pp. 1–4.

[24] Isaac Skog *et al.* "Inertial sensor arrays, maximum likelihood, and cramér–rao bound". *In*: *IEEE Transactions on Signal Processing* 64.16 (2016), pp. 4218–4227.

[25] Anderson Wedderhoff Spengler. *Técnica de condicionamento e processamento de sinais para girômetros a fibra óptica com malha fechada óptica*. Tech. rep. UFSC, 2014. Available from: http://repositorio.unicamp.br/jspui/bitstream/REPOSIP/260731/1/Spengler_AndersonWedderhoff_D.pdf.

[26] STonlineMedia. *MEMS Gyroscopes*. 2017. Available from: https://www.youtube.com/watch?v=l75IiNVRdfg.

[27] M Tanenhaus *et al.* "Miniature IMU/INS with optimally fused low drift MEMS gyro and accelerometers for applications in GPS-denied environments". *In*: *Proceedings of IEEE/ION PLANS 2012*. 2012, pp. 259–264.

[28] Jessica Azevedo Valdemir Carrara Mateus Pereira. *Attitude sensors calibration and modeling for cubesats*. 2020.

[29] Verena Venek, Wolfgang Kremser, and Cornelia Schneider. "Towards an IMU Evaluation Framework for Human Body Tracking." *In*: *eHealth*. 2018, pp. 156–163.

[30] Liang Xue *et al.* "Noise reduction of MEMS gyroscope based on direct modeling for an angular rate signal". *In*: *Micromachines* 6.2 (2015), pp. 266–280.

[31] Zheng You. *Space Microsystems and Micro/nano Satellites*. Micro and Nano Technologies. Butterworth-Heinemann, 2018, pp. i–iii. DOI: https://doi.org/10.1016/B978-0-12-812672-1.00011-4. Available from: https://www.sciencedirect.com/science/article/pii/B9780128126721000114.

[32] Jianwei Zheng *et al.* "IMU performance analysis for a pedestrian tracker". *In*: *International Conference on Intelligent Robotics and Applications*. Springer. 2017, pp. 494–504.